MAGHEMITE NANOSHEETS AS HIGH PERFORMANCE CATHODES FOR LITHIUM-ION BATTERIES

by

Sibo Niu, M.S.

A thesis submitted to the Graduate Council of
Texas State University in partial fulfillment
of the requirements for the degree of
Master of Science
with a Major in Chemistry
December 2016

Committee Members:

Christopher P. Rhodes, Chair

Benjamin Martin

Jennifer Irvin

FAIR USE AND AUTHOR'S PERMISSION STATEMENT

Fair Use

Duplication Permission

ACKNOWLEDGEMENTS

This work was supported by the National Science Foundation (DMR-1205670). The author would like to thank to Ryan McFeron, Dr. Fernando Godinez-Salomon, Brian Chapman, Dr. Joseph Tracy and Dr. Christopher P. Rhodes who all contributed to the work. Thesis committee members to be recognized for significant constructive input are Dr. Benjamin Martin, Dr. Jennifer Irvin and most of all Dr. Christopher Rhodes.

TABLE OF CONTENTS

Page

LIST OF TABLES

Table **Page**

LIST OF FIGURES

Figure **Page**

LIST OF ABBREVIATIONS

Abbreviation	Description
2D	Two-dimensional
BET	Brunauer–Emmett–Teller
CV	Cyclic voltammetry
DEC	Diethyl carbonate
EC	Ethylene carbonate
EMC	Ethyl methyl carbonate
EG	Ethylene glycol
SEM	Scanning electron microscope
TEM	Transmission electron microscopy
TGA	Thermogravimetric analysis
TMDs	Transition metal dichalcogenides
TMOs	Transition metal oxides
XRD	X-ray powder diffraction

ABSTRACT

Iron oxides as cathodes for lithium-ion batteries typically show low specific capacities and poor rate capabilities. Two-dimensional (2D) materials show high potential for energy storage materials because of their large surface area, no/small solid lithium ion diffusion, and electron confinement that result in increased surface-based charge storage through higher electrode surface areas and improved electronic conductivities. In this work, iron oxide, γ-Fe_2O_3, nanosheets were prepared and tested as cathodes for lithium-ion batteries. The results show that γ-Fe_2O_3 nanosheets exhibit better electrochemical properties with higher capacities and improved rate capabilities compared with γ-Fe_2O_3/ α-Fe_2O_3 nanoparticles. The improved electrochemical performance is attributed to their 2D structure that provides a large surface area, primarily surface-based charge storage, and higher electronic conductivity. The γ-Fe_2O_3 nanosheets prepared using a facile reaction are potential cathode materials for next generation, low-cost lithium-ion batteries.

1. BACKGROUND

1.1 Lithium-ion Batteries

Currently, rapid depletion of non-renewable fuels and increasing environmental concerns are motivating the development of clean, renewable, and sustainable sources of energy as well as efficient methods of energy storage and conversion. In this prospect, lithium-ion batteries are considered as effective energy storage devices for mobile devices, including cell phones, laptops, tablets and portable medical machines that completely change global communication.[1-3]

Lithium-ion batteries are suitable for electric vehicles because of their capacity for higher energy and power output per unit of battery mass compared with other technologies, such as lead acid, Ni-Cd and Ni-MH batteries.[4-6] The global electric car market will expand tremendously in the near future. For example, the German government has set the target of one million electric vehicles on the road by 2020, and six million by 2030.[7] However, mass manufacture and promotion of electric and hybrid vehicles require next-generation lithium-ion batteries with not only improved safety, high capacity, good rate capability, long cycling life but also relatively low cost to enable a price reduction in electric and hybrid vehicles.

Lithium-ion batteries have four major components: cathode (positive electrode), anode (negative electrode), electrolyte and separator. Commercial anode materials are primarily graphite. Commercial electrolytes, such as 1.0 M $LiPF_6$ in EC/EMC (50: 50) or in EC/DEC (50: 50), transfer the ionic component of the chemical reaction within the cell.[8] For separators, microporous polymer membranes are used to isolate the cathode and anode, which allows the exchange of lithium ions between the two electrodes but not

electrons[9]. The mechanism of a rechargeable lithium-ion battery is shown in Figure 1.[10] During the charging process, both anode and cathode are connected to external electronic supply. Internally, the lithium ions are extracted from cathode to anode during charging, and at the same time, the electrons externally are transferred along same direction from cathode to anode. After the charging process, electric energy is stored in the battery in the form of chemical energy, and the anode side has a higher chemical potential than that of the cathode counterpart. When discharged, lithium ions are transported from the anode to cathode, and simultaneously, electrons travel within the external circuit to power device. For example, $LiCoO_2$, most commonly used in lithium-ion batteries, experience electrochemical lithium extraction with compensating electrons, leading to the formation of $Li_{1-x}CoO_2$ as follows:

$$LiCoO_2 \leftrightarrow Li_{1-x}CoO_2 + xLi^+ + xe^- \quad (1)$$

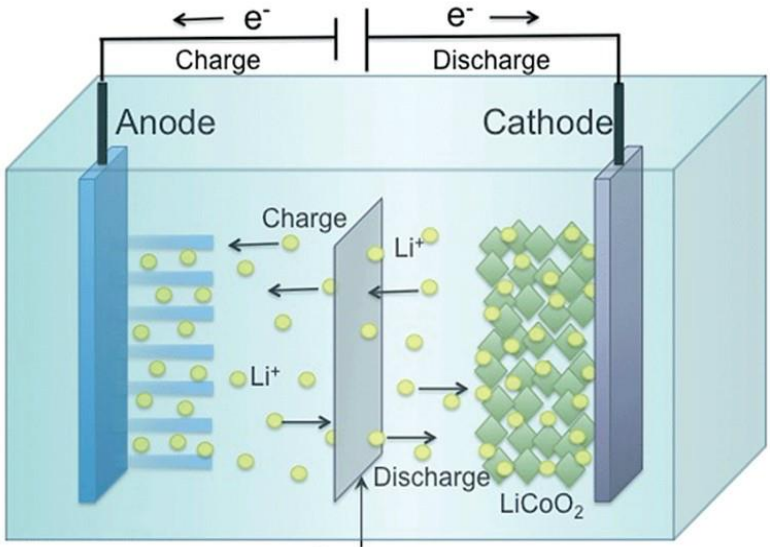

Figure 1. The charging and discharging processes that occurs in a rechargeable lithium-ion battery.[9]

1.2 Cathode Materials

Commercial cathode materials primarily include $LiCoO_2$, $LiFePO_4$, $LiNi_xCo_yAl_zO_2$, $LiNi_xMn_yCo_zO_2$ (NMC) and $LiMn_2O_4$.[11] During the past two decades, the $LiCoO_2$ cathode has been widely used in portable electronics.[12] $LiCoO_2$ was first identified as a lithium intercalation electrode in 1980 by Goodenough *et al*. and introduced as commercial cathode materials by Sony Company in 1991, which marked the beginning of the rapid expansion of lithium-ion batteries as a power source for portable electronic devices.[13-14] Overall, $LiCoO_2$ exhibits excellent cyclability at room temperature with a specific capacity in the range of 137 to 140 mAh g^{-1}, whereas the theoretical capacity of $LiCoO_2$ is 273mAh g^{-1}.[15] However, the high cost of $LiCoO_2$, \$20-50/kg, and its limited rate capacity have limited the use of Li-ion batteries for large-scale applications in transportation and stationary energy storage. In addition, due to its toxicity, $LiCoO_2$ has negative health and environmental impacts, including ecological toxicity, and respiratory-related health impacts.[16]

In addition to $LiCoO_2$, $LiFePO_4$ has been recently developed for commercial applications because of low toxicity and high safety.[17] The theoretical capacity of $LiFePO_4$ is 170 mAh g^{-1}.[18] However, as a result of its low electronic conductivity, the commercial use of $LiFePO_4$ cathode material has been hindered.[19] In addition, $LiFePO_4$ still suffers from relatively high cost, \$32-40/kg.

$LiMn_2O_4$ is the third most popular cathode material for lithium-ion batteries. In comparison with $LiCoO_2$, $LiMn_2O_4$ has an abundant materials source, and has a theotical capacity of 148 mAh g^{-1}.[20] However, unfortunately, $LiMn_2O_4$ has a rapid capacity fading problem during cycling, which has been an obstacle to its commercialization.[21] In

addition to $LiCoO_2$, $LiFePO_4$ and $LiMn_2O_4$, other materials, such as $LiMn_{1-x-y}Ni_xCo_yO_2$, $LiMn_{0.5}Ni_{0.5}O_2$, $LiMn_{1.5}Ni_{0.5}O_4$ spinel and $LiNi_{1-x}MO_2$ (M = a third metal, Co, Al) are currently being explored.[22-24] However, none of these has been used in commercial applications due to relatively high cost and/or poor electrochemical properties. Therefore, the development of low-cost cathodes for lithium ion batteries with high capacity, excellent cycling stability, high rate, and improved safety is urgently needed.

1.3 Iron Oxides

During the past several decades, iron oxides have attracted significant interest as potential cathode materials in lithium-ion batteries due to their low cost, environmental friendliness and natural abundance.[25] Iron oxide compounds are widespread in nature. Formation of ferric oxide occurs in both terrestrial and marine environments because of aerobic weathering of magmatic rocks.

The most common phases of iron oxide are hematite, magnetite and maghemite. Hematite, α-Fe_2O_3, is the most stable iron oxide with semiconducting properties under ambient conditions and has wide usage in solar water splitting, water treatment, photocatalysis, lithium-ion batteries and gas sensors.[26] The crystal structure of hematite is a rhombohedrally-centered hexagonal closed packed lattice.[27] As shown in Figure 2, Fe^{3+} ions occupy two-thirds of the octahedral sites surrounded by six oxygen atoms.[28]

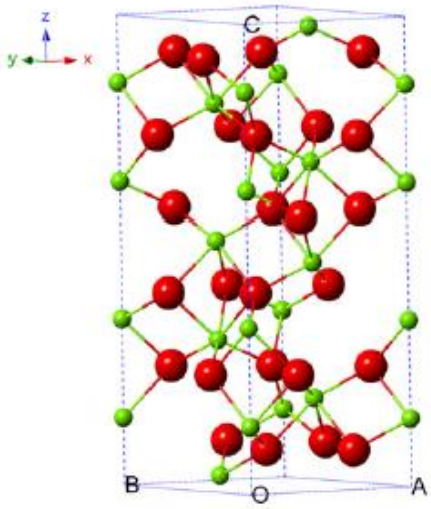

Figure 2. Crystal structure of hematite (the green ball is Fe^{3+} and the red ball is O^{2-}).[25]

Magnetite, Fe_3O_4, has a cubic crystal structure with Fd3m space group. In the structure of magnetite, shown in Figure 3, 32 O^{2-} ions form a closed packed cubic unit cells along the (111) direction.[28] All of the Fe^{2+} ions in the crystal occupy half of the octahedral sites and the Fe^{3+} fill the remaining octahedral sites and the tetrahedral sites.

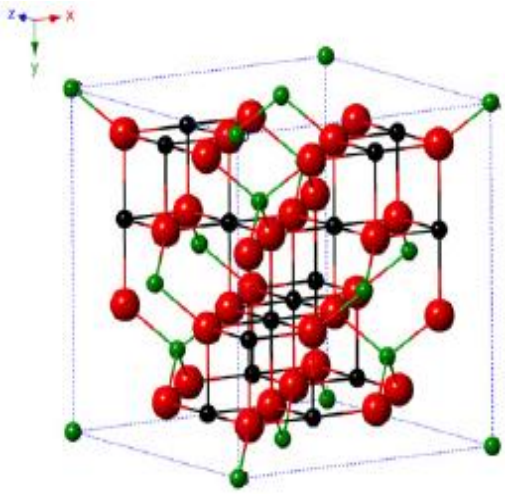

Figure 3. Crystal structure of magnetite (the black ball is Fe^{2+}, the green ball is Fe^{3+} and the red ball is O^{2-}).[25]

As shown in Figure 4, maghemite, γ-Fe_2O_3, has a similar cubic crystal structure to magnetite, where Fe^{3+} cations are distributed in 16 octahedral and 8 tetrahedral sites in the O^{2-} closed packed hexagonal crystal structure.[28]

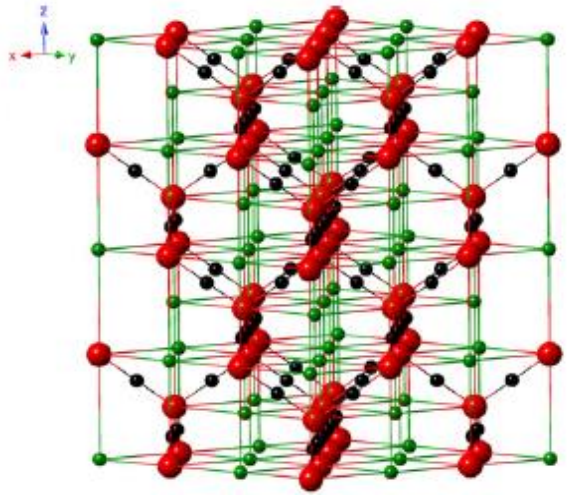

Figure 4. Crystal structure of maghemite (the black ball is Fe^{2+}, the green ball is Fe^{3+} and the red ball is O^{2-}).[25]

Figure 5 shows the XRD peak from the standard powder diffraction files of α-Fe_2O_3 (PDF#33–0664), Fe_3O_4 (PDF#19–0629) and γ-Fe_2O_3 (PDF#39–1346), and it can be found that peaks of γ-Fe_2O_3 are similar to these of Fe_3O_4 with some peaks shifted slightly towards higher angles.

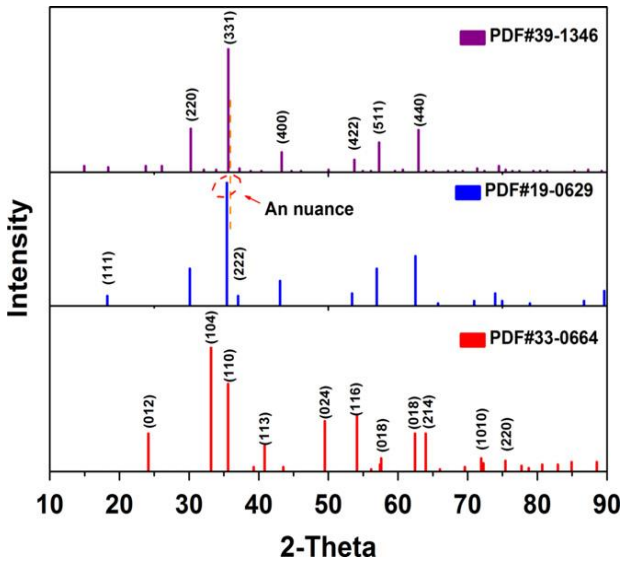

Figure 5 The XRD peak lines from standard powder diffraction files of α-Fe_2O_3, Fe_3O_4 and γ-Fe_2O_3.[25]

However, unlike Fe_3O_4, γ-Fe_2O_3 has cation vacancies either randomly occupied in the tetrahedral and octahedral sites or distributed only on the octahedral sites,[29-31] which also can be represented as $(Fe^{3+})[Fe_{1.67}^{+}\square_{0.33}]O_4$ in which (Fe^{3+}) and $[Fe_{5/3}]$ designates tetrahedral and octahedral coordination, respectively and □ represents a cation vacancy with octahedral coordination.[32] Therefore, in addition to XRD characterization, Raman spectroscopy, as an analytical method of probing local structure, has been conducted to differentiate Fe_3O_4 and γ-Fe_2O_3 phases.[33-34] Figure 6 shows the Raman spectra of Fe_3O_4 (top) and γ-Fe_2O_3 (bottom) between 585 and 805 cm^{-1}.[35] For maghemite, there are two Raman bands, one is at 667 cm^{-1}, which corresponds to A_{1g} band and FeO_4 tetrahedra vibrations mode without cation vacancies. Another band is at 721 cm^{-1}, corresponding to local Fe-O structures in the vicinity of cation vacancies in γ-Fe_2O_3.[34, 36] However, Fe_3O_4 has only one predominant band at 667 cm^{-1}.

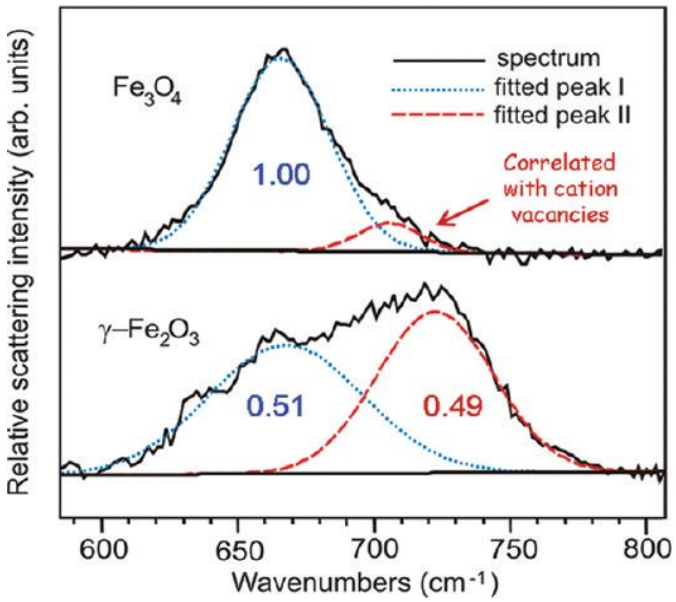

Figure 6. Raman spectra of Fe_3O_4 (top) and γ-Fe_2O_3 (bottom).[34]

Due to the similarity in crytal structures of iron oxides, different phases of iron oxides can converted by oxidation or reduction.[28] For example, γ-Fe_2O_3 is able to be transformed to α-Fe_2O_3 by thermal treatment in air.[37] Conversely, certain milling conditions can induce the direct transformation from α-Fe_2O_3 to γ-Fe_2O_3.[38] Maghemite (γ-Fe_2O_3) can be obtained by oxidizing Fe_3O_4 in air.[39]

1.4 Iron Oxide Cathodes

Even though iron oxides have attracted particular attention because of their non-toxicity, high abundance, and low cost, the use of iron oxide cathodes is hindered by their low specific capacity, poor rate capability and capacity fading over extended cycling.[40-41] For Fe_2O_3, during the charging process, Li^+ ions intercalate into Fe_2O_3 accompanied with electrons and Fe^{3+}/Fe^{2+} conversion. The route is inverted as discharge takes place. The charge/discharge can be represented by the following equation.

$$Fe_2O_3 + xLi^+ + xe^- \leftrightarrow Li_xFe_2O_3 \quad (2)$$

The theoretical capacity for a one electron process per iron center ($Fe^{3+/2+}$) corresponding to x=2 in the above equation is 323 mAh g^{-1} for Fe_2O_3 and 231 mAh g^{-1} for Fe_3O_4, which is significantly higher than current commercial cathodes (e.g. 140-170 mAh g^{-1}).[42-45]

Despite their high theoretical capacities, iron oxide cathodes typically exhibit very low practical capacities. Prior work reported the specific capacity of iron oxide (γ-Fe_2O_3) nanoparticles was between 1-15 mAh g^{-1}.[46] The specific capacity of Fe_3O_4 nanoparticles with particle sizes of ~400 nm was reported to be 5-7 mAh g^{-1}.[47]

Various approaches have been explored to increase the capacities of iron oxide cathodes. Cation defects have been shown to significantly influence the electrochemical properties of iron oxides.[48-49] Substitution of a fraction of the Fe^{3+} sites with highly oxidized Mo^{6+} to generate more cation vacancies was been used to increase the capacity of defect spinel γ-Fe_2O_3 nanoparticles.[46] Vanadium (V^{5+}) substitution into iron oxide aerogels has also been demonstrated to result in increased cathode capacities.[49]

The effect of particle size on the electrochemical properties of α-Fe_2O_3 nanoparticles and γ-Fe_2O_3 nanoparticles has been reported.[50-51] The specific capacity of α-Fe_2O_3 nanoparticles with 20 nm diameters (60-70 mAh g^{-1}) was significantly higher than that of the capacity of 500 nm α-Fe_2O_3 particles (15 mAh g^{-1}).[50] Based on the results, it was hypothesized that decreasing the size of iron oxide nanoparticles could enhance the specific capacity of Li-ions due to higher surface area. Prior work showed that the specific capacities of γ-Fe_2O_3 increased (up to 130 mAh g^{-1}) with decreasing particle size.[51]

1.5 Two-dimensional Nanomaterials

Besides 3D cube-like nanostructures, during the past several decades, research has been aimed at developing various types of nanostructures to maximize the electrochemical properties, as shown in Figure 7.[52] 1D nanostructures, such as nanotubes or nanowires, has hollow structures that can facilitate the transport of electrons and provide improved electronic conductivity.[53-54]

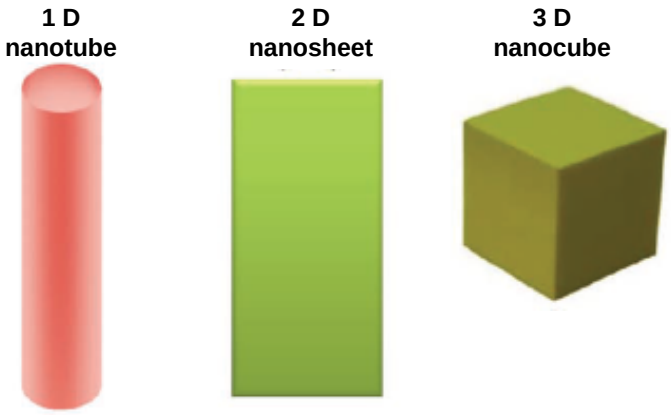

Figure 7. Structures of the nanotube, nanosheet and nanocube.[50]

Two-dimensional (2D) materials are materials where the atomic organization and bond strength along two-dimensions are similar and much stronger than along a third dimension.[55] Compared to bulk materials, two-dimensional materials consisting of single or a few layers of atoms with quantum confined electrons have been shown to exhibit superior electronic, optical, mechanical, chemical and thermal properties.[56-57] The development of nanosheets as a class of two-dimensional material with single or many layers, dates as far back as the 1950s.[55, 58] The term "nanosheets" was initially defined and used by Sasaki *et al*. in 1996 to represent the unique features of both molecular thickness and extremely high 2D anisotropy. Besides layered 2D material, various 2D platelet- or leaf-like nanomaterials are also sometimes called nanosheets.[59]

Traditional sheet-like nanomaterials are graphene nanosheets that are two-dimensional layers with one-atomic thickness and consist of strongly bonded carbon networks. Compared to their host material, graphite powder, with typical surface area smaller than 900 m^2/g, graphene nanosheets have much higher theoretical surface areas over 2600 m^2/g and superior electrical conductivities.[60-61] In addition, graphene nanosheets exhibit mechanical strength, ease of functionalization, and potential for mass production.[62-64] The combination of all these characteristics make graphene nanosheets a possible competitive candidate for electrode material for energy conversion and strorage devices, such as fuel cells, solar cells and Li-ion batteries.[61]

1.6 Two-Dimensional Transition Metal Oxides

The family of 2D materials has grown steadily and is no longer limited to graphene nanosheets. Other 2D crystals, such as transition metal dichalcogenides (TMDs) (for example, WS_2, MoS_2, and WSe_2) and 2D transition metal oxides (TMOs) (for example, SnO_2 , TiO_2, NiO, and CoO_2) have been reported.[65-69] Typically, rather than using micron-sized particles or nanoparticle forms, 2D transition metal oxides have a number of key features that can facilitate energy storage including (i) quantum confinement that can result in orders of magnitude higher electronic conductivity, (ii) significant available surface area beyond that of nanoparticles and nanotubes, (iii) surface-based charge storage that avoids slow solid-state diffusion, (iv) surface-controlled properties, and (vi) the ability to accommodate structural strain and substantial curvature without structural breakdown.[70-73]

So far, synthesis of atomically thin, 2D TMOs with uniform properties has been primiarly achieved by two methods: (*i*) chemical exfoliation, that is delamination of bulk

layered compounds into single layers, and (*ii*) bottom-up synthesis with the aid of proper surfactant and solvents to direct the sheet-like structure grown.

Top-down chemical exfoliation methods are shown in Figure 8. Atomically thin flakes can be peeled from their parent bulk crystals by micromechanical cleavage. For example, atomically thin WO_3 sheets are derived from hydrated tungsten trioxide by micromechanical cleavage.[74] MnO_2 nanosheets can be obtained via delamination of a layered manganese oxide.[75] Other exfoliated transitional metal oxide nanosheets include $Co(OH)_2$, $TiNbO_5$, Ti_2NbO_7, $TiTaO_5$, etc.[76-77]

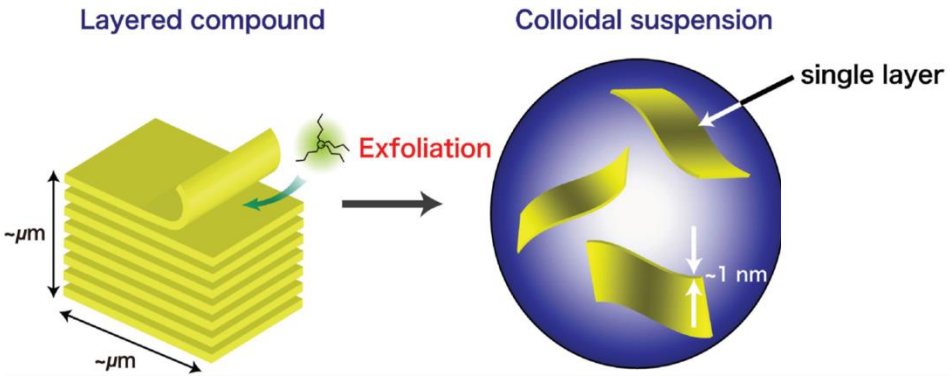

Figure 8. Schematic model illustrating the exfoliation of a layered compound into nanosheets.[55]

However, one problem is that monolayers obtained by micromechanical exfoliation, also known as micromechanical cleavage, are usually accompanied by flakes with variety of size, shape, thickness and lateral dimension.[78-79] Another problem is that only a few 2D metal oxides are suitably layered host crystals. In other words, only 2D platelets/nanosheets that are weakly stacked to form 3D bulk materials can be obtained via the exfoliation method.[80]

Thus, the bottom-up solution-phase strategy to control the synthesis of 2D metal oxides nanostructures seems to be more desirable to meet the growing requirement for

such 2D TMOs. Some transition metal oxides, such as NiO, anatase TiO_2, MnO_2 and ZnO nanosheets have been synthesized via solution-phase strategy with appropriate solvents and surfactants.[81-84]

One of the solvents that is most frequently used for bottom up synthesis of TMO nanosheets is ethylene glycol (EG). EG is a strong reducing agent with a relatively high boiling point and has been widely used in the polyol process to provide monodispersed fine metal or metal oxide.[85-86] In addition, it has been reported that EG can participate in the role of both co-surfactant and co-solvent in the surfactant–water system and plays a very crucial role in the formation of ultrathin 2D transitional metal oxide nanosheets.[87-88] For example, without EG, even adding PEO_{20}–PPO_{70}–PEO_{20}, ZnO nanoparticles are obtained instead of nanosheets.[80]

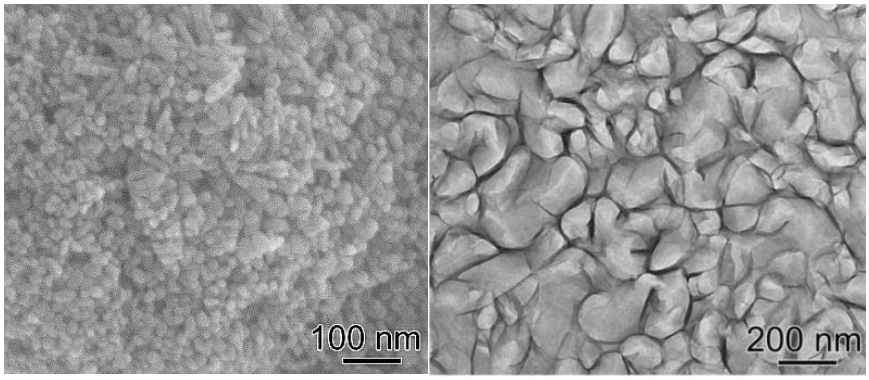

Figure 9. Morphology of ZnO nanomaterial with (right) or without (left) EG.[77]

1.7 Two-dimensional Iron Oxides

Iron oxide nanosheets can be synthesized by chemical exfoliation and solution phase synthesis.[89-91] For example, layered Fe^{III} oxide nanosheets, shown in Figure 10, have been prepared by a two-step reaction: (*i*) anion exchanging layered Fe^{II}/Fe^{III} hydroxide chloride with dodecanoate, followed by (*ii*) solid state oxidation and exfoliation.[89]

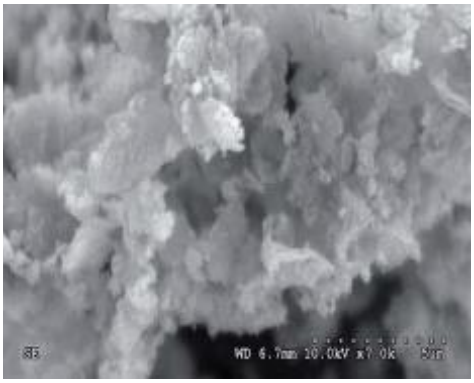

Figure 10. Scanning electron microscope (SEM) image of the layered Fe^{III} oxide nanosheets after exfoliation.[86]

However, obtaining iron oxide/hydroxide nanosheets via solution-phase methods is more popular, as has been shown with $Fe(OH)_2$, Fe_3O_4, δ-FeOOH, amorphous FeOOH and γ-FeOOH nanosheets.[91-97] Iron hydroxide, $Fe(OH)_2$, is one of the hydroxides of iron that has layered crystal structure with a space group of P3m1.[91, 98] Fe atoms occupy inside the octahedral holes of every layer between the anion layers A and B of the ABAB stacking sequence. The layered structure of ferrous hydroxide makes it tend to form sheet- or plate-shaped crystals.[91]

$Fe(OH)_2$ can be obtained by reacting iron (II) sulphate heptahydrate ($FeSO_4.7H_2O$) with sodium hydroxide (NaOH). The equation can be written as follows:[99]

$$FeSO_4 + 2NaOH \leftrightarrow Fe(OH)_2 + Na_2SO_4 \quad (3)$$

The reaction can be described by x mol/L of $FeSO_4$ with y mol/L of NaOH give rise to the initial reaction. The initial ratio of preparation of the reacting chemicals can be designated as R, The equation can be written as follows: [99]

$$R = [FeSO_4]/[NaOH] = [Fe^{2+}]/[OH^-] = [SO_4^{2-}]/[OH^-] = x/y \quad (4)$$

When the reaction occurs in basic conditions, for example, $R < 0.5$ or $y > 2x$, all Fe^{2+} ions precipitate as $Fe(OH)_2$ and some OH^- ions are left in the solution. The equation of the reaction is as follows: [99]

$$xFeSO_4 \cdot 7H_2O + yNaOH \leftrightarrow xFe(OH)_2 + xNa_2SO_4 + (y-2x)Na^+ + (y-2x)OH^- +7H_2O \quad (5)$$

If $R > 0.5$ or $y < 2x$, the reaction occurs in acidic conditions. Different from the basic conditions, all initial OH^- ions are consumed to precipitate $Fe(OH)_2$ with excess Fe^{2+} ions in the solution. The initial reaction is as follows: [99]

$$xFeSO_4 \cdot 7H_2O + yNaOH \leftrightarrow y/2Fe(OH)_2 + y/2\ Na_2SO_4 + (x-y/2)Fe^{2+} + (x-2y)\ SO_4+7H_2O \quad (6)$$

The pH value is essential in this reaction according to a prior study.[100] It has been reported that within different pH ranges, the product is variable. Fe^{2+} ions can be hyrolyze in water and condense in alkaline solution (pH>12) to produce $Fe(OH)_2$, as shown in Figure 11. At first, Fe^{2+} ions are dissolved in water molecules and can be represented by the following equation.[100]

$$Fe^{2+}+6H_2O \leftrightarrow [Fe(OH_2)_6]^{2+} \quad (7)$$

Then water behaves as a Lewis base, and some electrons transfer from the water molecule to the metal cation.

$$[Fe(OH_2)_6]^{2+} + H_2O \leftrightarrow [Fe(OH_2)_5(OH)]^+ + H_3O^+ \quad (8)$$

After Fe^{2+} hydrolysis, the hydroxylated complexes can condense by two steps: one is forming hydroxo bridges between Fe^{2+} ions, another is oxolation, formation of oxo bridges between Fe^{2+} ions, as represented by the following equations.[100]

$$[Fe(OH_2)_5(OH)]^+ + [Fe(OH_2)_6]^{2+} \leftrightarrow [(OH_2)_5\ Fe(OH)Fe(OH_2)_5]^{3+} + H_2O \quad (9)$$

$$2Fe(OH_2)_5(OH)]^+ \leftrightarrow [(OH_2)_4\ Fe(OH)_2Fe(OH_2)_5]^{2+} + H_2O \quad (10)$$

$$2Fe(OH_2)_5(OH)]^+ \leftrightarrow [(OH_2)_5\ FeOFe(OH_2)_5]^{2+} + H_2O \quad (11)$$

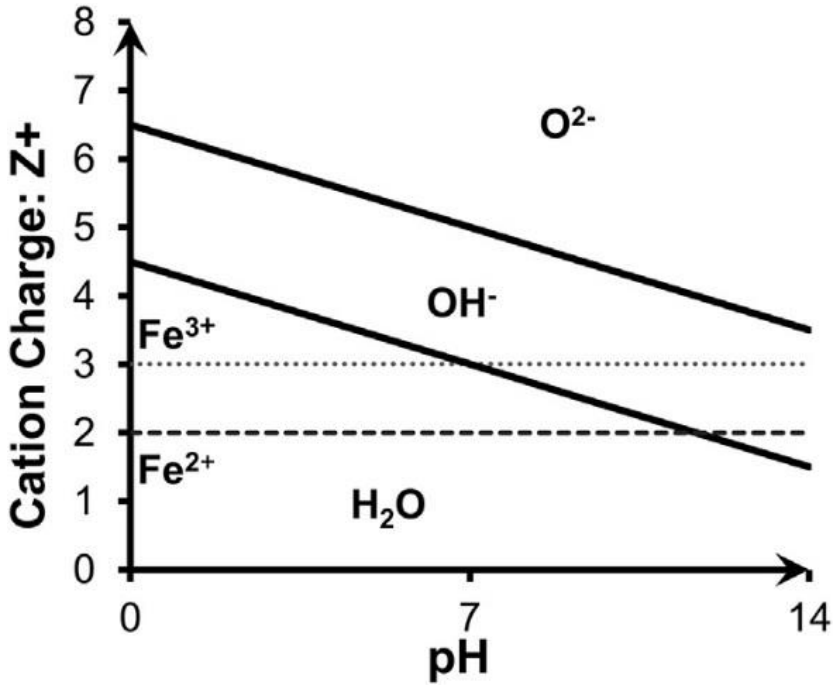

Figure 11. Charge-pH diagram.[96]

However, despite having a naturally layered structure, $Fe(OH)_2$ does not form large sheet-like structures without certain amounts of EG.[91] Without EG, the morphology of the $Fe(OH)_2$ obtained in pure aqueous solution is mixture of plate/rod structure (Figure 12b). By contrast, the $Fe(OH)_2$ precipitates exhibit nanosheet structures after adding EG (Figure 12a). This contrast could be attributed to the a strong chelating ability of EG, which can chelate transiton metal ions, such as Ti^{4+} and Fe^{2+}, in certain planes and facilitate formation of metal oxide nanosheets.[101-102]

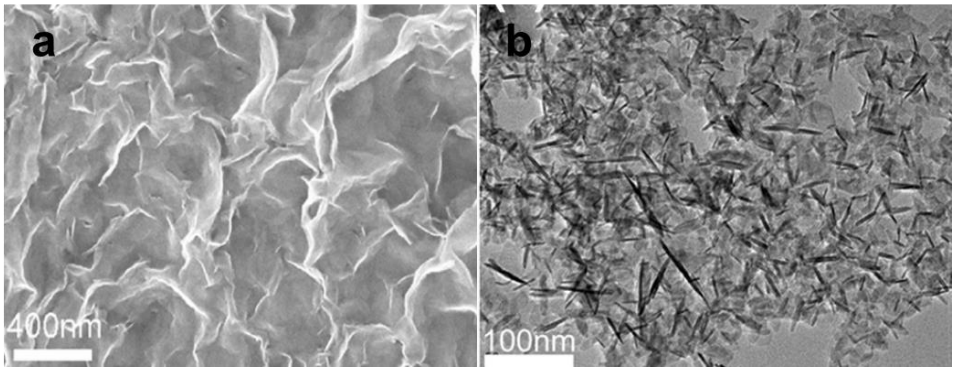

Figure 12. Fe $(OH)_2$ (a**)** SEM of Fe $(OH)_2$ obtained in the EG-H_2O mixture.

(b) TEM of Fe $(OH)_2$ obtained in the pure water.[91]

1.8 Iron Oxide Nanosheets as Anodes for Lithium Ion Batteries

Iron oxides/hydroxide nanosheets, such as Fe_2O_3 and amorphous FeOOH, have recently received increased attention as very promising anode materials for lithium-ion batteries.[93, 97] Generally, as anodes, using Fe_2O_3 as an example, the reaction equation can be described as follows:[103]

$$Fe_2O_3+6Li^{+}+ 6e^{-} \leftrightarrow 3Li_2O+2Fe \quad (7)$$

The theoretical capacity of iron oxides is very high within the voltage window of 0.01 to 3.0 V vs Li, about 1000 mA g^{-1}. Iron oxide nanosheets have been evaluated as anode materials and have shown very high capacities and an improved electrochemical

performance compared to nanoparticles.[93, 97, 104] For example, amorphous iron oxyhydroxide nanosheets as anode show superior rate capabilities, specifically, discharge capacities is as high as 642 mAh g^1 at 2C.[93] Accordingly, α-Fe_2O_3 nanosheet anodes deliver reversible capacities of 1327 mAh g^{-1}, which is much higher than that of α-Fe_2O_3 nanoparticle anodes (1006 mAh g^1) at 1C current rate.[104] However, no prior studies of iron oxide nanosheets as cathode materials within voltage range between 1.5-4.2V vs Li for Li-ion batteries have been reported to date.

1.9 Motivation of the Research

The motivation of the project is to improve the specific capacity and rate capability of iron oxides through synthesis of two-dimensional iron oxide, γ-Fe_2O_3, nanomaterials. Two-dimensional materials show high promise for energy storage because of their large surface area, no/small solid lithium ion diffusion and electron confinement, which can increase the contact area with the electrolyte and improve the ionic and electronic conductivity. γ-Fe_2O_3 has cation vacancies, either randomly occupying in the tetrahedral and octahedral sites or preferrentially distributing only on the octahedral sites, which can benefit the insertion of lithium-ions. The research objectives were to syntheize γ-Fe_2O_3 nanosheets, detemrine their electrochemical properties, and compare the performance with that of Fe_2O_3 nanoparticles. The factors that influence the electrochemical performance of iron oxides were also evaluated. The overall goal was to develop low-cost γ-Fe_2O_3 nanosheets with high electrochemical performance as cathodes for Li-ion batteries.

2. MATERIALS AND METHODS

2.1 Materials

Sodium hydroxide (NaOH, 97%, EM Science), ethylene glycol ($C_2H_6O_2$, 99%, BDH) and Iron (III) oxide, magnetic (γ-Fe_2O_3, >98%, Alfa Aesar) was obtained from VWR International (Radnor, PA, USA). Iron (II) sulfate heptahydrate ($FeSO_4 \cdot 7H_2O$, 99%), iron (II, III) oxide (Fe_3O_4, 95%), iron (III) oxide (α-Fe_2O_3, $\geq$ 95%), sulfuric acid (H_2SO_4, 95%-98%), ethyl alcohol (C_2H_6O, 99.5%) and hydrogen peroxide (H_2O_2, 30%) were obtained from Sigma-Aldrich (St. Louis, MO, USA).

2.2 Iron Oxide Nanomaterial Synthesis

Iron oxide (FeO_x) nanosheets were synthesized by modification of reported synthesis methods for δ-FeOOH synthesis[91-92]. To synthesize the FeO_x nanosheets, 0.5 g of sodium hydroxide (NaOH) was dissolved in 5 mL deionized (DI) water ($\geq$ 13 MΩ/cm), and then 50 mL ethylene glycol (EG) was added to the solution. Separately, a solution of 0.04g iron (II) sulfate heptahydrate ($FeSO_4 \cdot 7H_2O$) was dissolved in 6 mL of 0.01 M sulfuric acid (H_2SO_4). Next, the NaOH/EG and the $FeSO_4/H_2SO_4$ aqueous solutions were degassed with argon for about 1 h. After this step, the $FeSO_4/H_2SO_4$ solution was slowly dropped into the NaOH/EG mixture using a pressure equalizing funnel and the reaction was allowed to proceed at room temperature for 3 h. The resulting material was collected by centrifuging at 5000 rpm for 15 minutes and then rinsed with a water/ethyl alcohol (1:1 volume ratio) mixture solution three times. The centrifuged and rinsed material was then suspended in 10 mL water/ethyl alcohol (1:1), and then 20 mL 3 wt % H_2O_2 was added to the suspension at a rate of 0.04 mL/min. Finally, the as-prepared FeO_x nanosheets were collected by centrifuge and dried under vacuum. Iron oxide (FeO_x)

nanorods were prepared by the same method except that 50 mL DI water was used as the solvent instead of EG. The dried FeO_x nanomaterials were either used as prepared or heated within a muffle furnace (Thermo, Thermolyne) to 200°C, 350°C or 450°C for 24 h in air using a ramp rate of 5ºC/ min.

2.3 Structural, Thermal, and Physical Characterization

XRD powder patterns of iron oxide samples were obtained with a Bruker D8 Focus Powder X-ray Diffractometer using Cu Kα radiation (λ=1.54060Å). Scans were recorded for 2θ values between 20 and 70°, using a step size of 0.0002° and integration of 5 s per step. The crystallite size was calculated using the Scherrer equation, $L= K\lambda/ (\beta \cos\theta)$, where L is the crystallite size, K is the Scherrer constant, λ is the x-ray wavelength, β is the line broadening at half the maximum intensity (FWHM), and θ is the Bragg angle.[105] The FWHM was determined from the experimental XRD pattern for either the (311) peak for γ-Fe_2O_3 or the (110) peak for α-Fe_2O_3.

Raman spectra were obtained with a Horiba LabRam HR Evolution Confocal Raman Spectrometer using a backscattering geometry and an 1800 mm grating. The 514-nm line of an argon-ion laser was focused through an Olympus microscope with a 50× lens. Spectra were obtained using a 24 second acquisition time and averaged over 50 accumulations. Laser-induced thermal effects were observed in prior Raman studies of iron oxides, and low laser powers were necessary to minimize spectral changes due to local heating[106]. To avoid sample degradation, the laser power was controlled below 1 mW using neutral density filters. Visual inspection of the samples, pre- and post-analysis, using white light illumination did not reveal any laser-induced changes. To further verify that the laser did not induce spectral changes, spectra were obtained at a laser power of

below 0.1 mW using the same acquisition and sampling conditions as above; no differences were observed compared to the spectra taken at 1 mW. The spectra of commercially available maghemite, magnetite and hematite were obtained for comparison to the synthesized nanomaterials.

To determine the morphology of iron oxide samples, TEM (transmission electron microscopy) images were obtained using a JEOL JEM 1200EXII microscope with an accelerating voltage of 120 k V. High resolution TEM images were obtained a JEOL 2010F operated at 200 kV. TEM samples were prepared on lacy carbon grids by depositing a solution of the dried powder suspended in isopropanol.

To determine the morphology of iron oxide samples, SEM (scanning electron microscope) images were obtained using a Helios NanoLab 400 DualBeam Field Emission Scanning Electron Microscope. The powder was dispersed into isopropanol and coated on an aluminum holder.

Thermogravimetric analysis (TGA) measures the amount of weight change of a material as a function of increasing temperature in an atmosphere, such as nitrogen, argon or air. To measure the weight loss of iron oxide nanosheets in air, TGA (TA Instruments Q50) was performed a constant heating rate of 10°C/min using air from room temperature to 500°C.

Surface areas and nitrogen adsorption/desorption isotherms of iron oxide samples were measured using a Micromeritics ASAP 2020 surface area and porosimetry analyzer. Samples were degassed at 100 °C for 16 h prior to characterization.

2.4 Electrochemical Measurements

Electrodes were fabricated from a slurry composed of 80 wt% iron oxide material (active material), 10 wt% conductive carbon (Timcal, Super C65), and 5 wt% binder (Aremka, Kynar HSV900) and 1-methyl-2-pyrrolidinone (NMP). The slurry was stirred overnight and then cast onto a cleaned aluminum foil current collector. The obtained electrode sheet was dried overnight within a fume hood and then transferred to a 60°C oven and allowed to dry overnight. Discs (0.5 inch in diameter) of the dried electrode sheets were then pressed out and dried in a vacuum oven at 120°C for 16 h.

For electrochemical testing, all coin cells (2032, Pred Materials) were fabricated in an inert atmosphere glovebox (argon, ≤1 ppm H_2O) using the electrode disc, a separator (Celgard 2500), a metallic lithium counter/reference electrode, and the electrolyte (1 M $LiPF_6$ in ethylene carbonate (EC): dimethyl carbonate (DEC) (EC/DEC=1:1 v/v) (Sigma-Aldrich).

Galvanostatic charge–discharge measurements were performed over a voltage range of 1.5 to 4.2 V vs Li on an Arbin Instruments BT2043 test station using mass normalized currents of 3.0-20 mA g^{-1} based on the active material mass, as described in the text. Cyclic voltammetry (CV) tests were performed at 0.1, 0.5, 1, 5 and 10 mV/s scan rate between 1.5 and 4.2 V with lithium counter and reference electrodes using an Arbin Instruments BT2043 test station.

2.5 Electrical Measurements

Conductivity measurements were performed in an HS Test Cell (Pred Materials International, Inc.) with a 10kg force spring. Two-point probe measurements were obtained using a constant voltage (± 0.1V) applied to the cell using an Arbin Instruments

BT-2043 potentiostat/galvanostat. Current was monitored until quasi-steady state was reached (~3 min). Electrical conductivity of the iron oxide samples, σ (S/cm), was calculated using the following equation:$\sigma(\mathrm{S/cm}) = l/RA$ and $R = V/I$, where voltage (V) is 0.1 and -0.1 mV and I (A) is the current, A (cm^2) is the area of pellet, and l (cm) is the thickness of the pellet. The thickness and diameter of pellet were measured using a micrometer (Mitutoyo, USA).

3. RESULTS AND DISCUSSION

3.1 Iron Oxide (γ-Fe_2O_3) Nanosheets Synthesis

Iron oxide nanosheets were synthesized in EG-water mixture or pure aqueous solution using a two-step process of (i) formation of iron hydroxide, $Fe(OH)_2$, nanosheets followed by (ii) treatment in H_2O_2 by using a modification of the method reported for δ-FeOOH nanosheets synthesis[92].

3.1.1 Synthesis of $Fe(OH)_2$ Nanosheets

To prepare the $Fe(OH)_2$ precusor, iron sulfate ($FeSO_4$. $7H_2O$) was reacted with sodium hydroxide (NaOH) solution with or without ethylene glycol. Without EG, the product shows a yellow brown color, whereas, the color of products obtained in mixture of water and ethylene glycol is white at the beginning and turns dark-green finally (Figure 13). Furthermore, TEM images of the product (Figure 14b) obtained in pure aqueous solution reveal the nanoparticle/rod structures. However, with EG, the samples exhibit sheet-like nanostructures, shown in Figure14a.

Therefore, it is demonstrated that ethylene glycol plays a very important role in formation of $Fe(OH)_2$ nanosheets. EG has been reported to have an effect on the synthesis of $LiFePO_4$ and δ-FeOOH nanosheets.[92, 101] Prior work suggested/reported that EG bonds with Fe^{2+} in the reactive FeO_5 group at the the (010) facets which is important in the formation of the nanosheet structure,[101] however further work is needed to understand the specific role of EG in the synthesis.

Figure 13. Products of Fe $(OH)_2$ with or without EG.

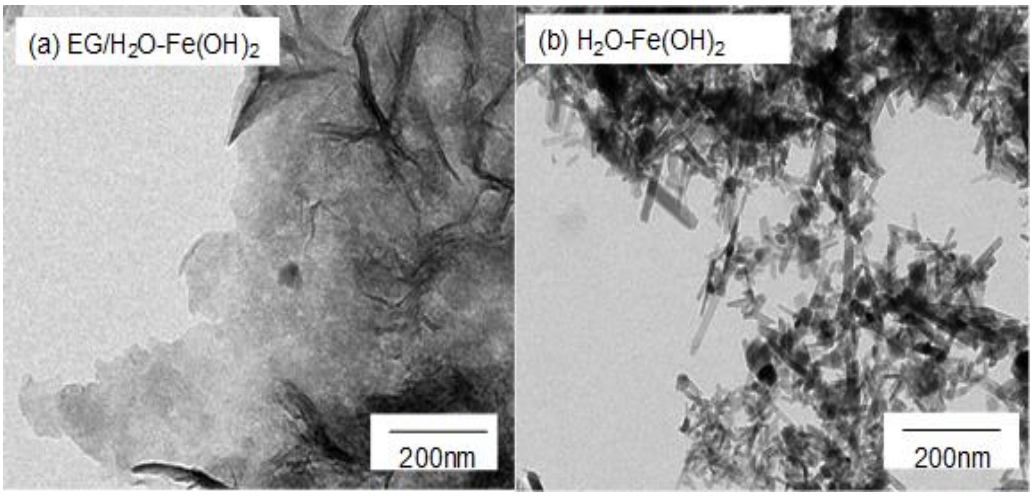

Figure 14. TEM of precursor FeO_x (a) FeO_x obtained in EG-water solution (b) FeO_x obtained in pure water.

3.1.2 XRD Analysis of the Synthesized FeO_x Nanomaterial

In the second step, the precipitates otained with or without EG were slowly oxidized by 3 wt% hydrogen peroxide (H_2O_2). Then the phases and morphology of products synthesized with or without EG were detetermined using XRD, Raman spectroscopy and TEM.

The atomic planes of a crystal cause an incident beam of X-rays to interfere with

one another as they leave the crystal. The phenomenon is called X-ray diffraction (XRD). This technique allows researchers to determine crystal phases and crystallite size of materials. XRD results for as-prepared FeO_x obtained in EG-water mixture and as-prepared FeO_x with pure aqueous solution are shown in Figure15. The XRD pattern of the as-prepared FeO_x obtained with EG is consistent with either Fe_3O_4, magnetite (JCPDS card no.75-0033) or γ-Fe_2O_3, maghemite (JCPDS card no. 39-1346),[107-108] whereas, most peaks of as-prepared FeO_x synthesized in pure aqueous solution are consistent with α-FeOOH, goethite (JCPDS card no. 29-713),[109] others are similar to Fe_3O_4/ γ-Fe_2O_3.

The Fe_3O_4 and γ-Fe_2O_3 phases are structurally very similar with unit cell "a" spacings of Δ=0.01 Å between the two phases.[110] While XRD can distinguish between these phases for highly crystalline materials, differentiating between Fe_3O_4 and γ-Fe_2O_3 using XRD is difficult for nanomaterials with broad XRD peaks.[111-112]

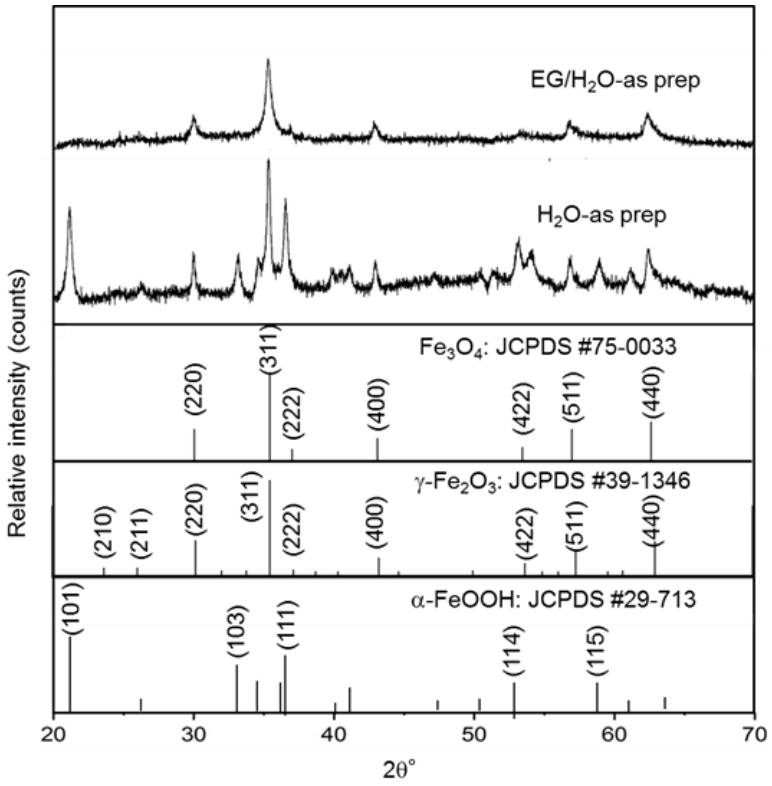

Figure 15. XRD of as-prep FeO_x (top) FeO_x obtained in EG-water solution (bottom) FeO_x obtained in pure water.

3.1.3 Raman Spectroscopy of the Synthesized FeO_x Nanomaterial

Raman spectroscopy is used to provide information about molecular vibrations and can be used for sample identification and quantitation. In addition to XRD, Raman spectroscopy was used to characterize iron oxide samples. While XRD relies on long-range order for structure identification, Raman spectroscopy probes the frequencies of vibrational modes which are sensitive to local structure. Since nanocrystalline materials typically have broad diffraction peaks due to the size of the particles, Raman spectroscopy is more useful than diffraction techniques to probe the structural differences between nanocrystalline iron oxides, particularly γ-Fe_2O_3 and Fe_3O_4.[113]

The Raman spectrum for as-prepared FeO_x (EG/H_2O-as prep) in the 200−900 cm^{-1} spectral region are shown in Figure 16 along with the spectra of commercially available γ-Fe_2O_3 and Fe_3O_4 for comparison. The frequencies of the Raman bands of the FeO_x-EG/H_2O-as prepared sample, particularly the broad band at 720 cm^{-1}, are consistent with γ-Fe_2O_3 rather than Fe_3O_4 as supported by the comparison with the commercial γ-Fe_2O_3 and Fe_3O_4 samples and previously reported spectra for these phases.[113] The local structure of as-prepared iron oxide nanosheets of γ-Fe_2O_3 which is more accurately represented as $(Fe^{3+})[Fe_{5/3}{}^{3+}\square_{1/3}]O_4$ supports that the as-prepared iron oxide nanosheets contain cation vacancies.[113]

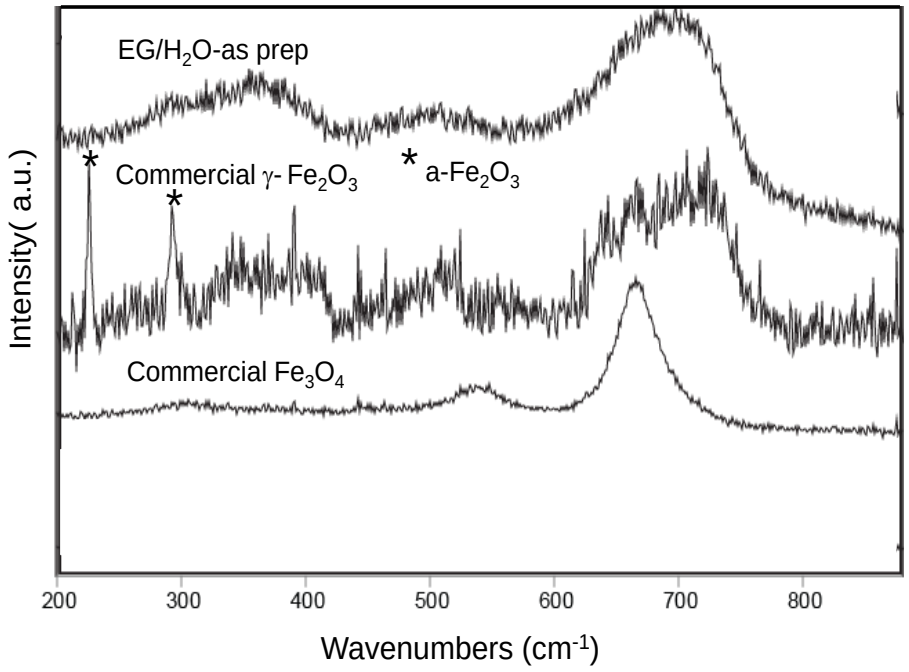

Figure 16. Raman spectra in the 200-900 cm^{-1} region for as-prepared FeO_x obtained in EG/H_2O solution, commercial γ-Fe_2O_3 and Fe_3O_4 samples.

3.1.4 Microscopy Analysis of the Synthesized FeO_x Nanomaterial

Structural information can be determined using X-ray diffraction and Raman spectroscopy, while transmission electron microscopy (TEM) is indispensable for characterization of morphology of nanocrystal materials. Figure 17a shows the TEM image of γ-Fe_2O_3 products prepared with EG/H_2O, and it can be seen that the products exhibit a sheet-like morphology with a thickness of 1-2 nm. However, TEM images of the α-FeOOH (Figure 17b) obtained in pure aqueous solution have nanoparticle/rod structures. Furthermore, the high resolution TEM image, shown in Figure 18, demonstrates the nanosheets consist of multiple crystallites. Observed lattice spacings of 4.8, 2.97 and 2.52 Å are consistent with the (111), (220) and (311) planes of γ-Fe_2O_3 (JCPDS card no. 39-1346), respectively. As discussed above, the assignment of the γ-Fe_2O_3 phase is further supported by Raman Spectroscopy. In addition, higher numbers of crystallites with lattice spacings of 2.52 Å were observed which indicates that the nanosheets consist of crystallites with a preferred (310) orientation perpendicular to the plane of the nanosheets.

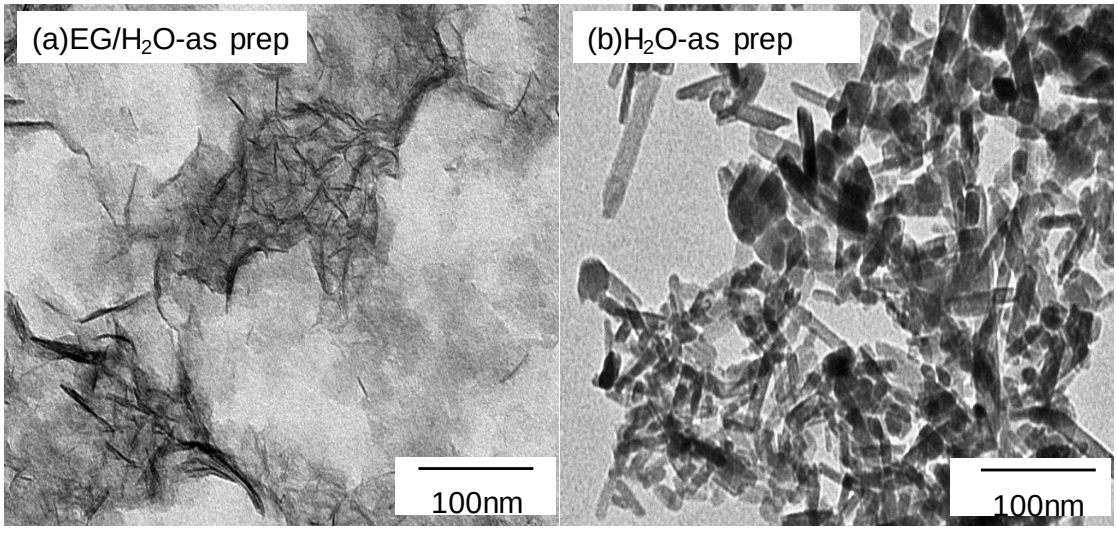

Figure 17.TEM of (a) γ-Fe_2O_3 nanosheets (b) α-FeOOH nanorods

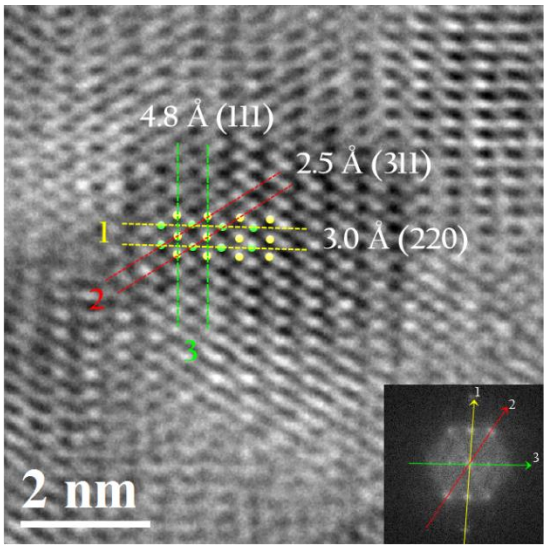

Figure 18. HRTEM image of γ-Fe_2O_3 nanosheets.

3.2 The Effect of Thermal Treatments on γ-Fe_2O_3 Nanosheets

3.2.1 TGA of γ-Fe_2O_3 Nanosheets

Thermogravimetric analysis (TGA) measures the amount of change in the weight of a material as a function of temperature in a controlled atmosphere. According to prior work, γ-Fe_2O_3 can be completely transformed into α-Fe_2O_3 phase when being annealled in air at 450 °C.[37] Therefore, in order to monitor weight change of as-prep γ-Fe_2O_3 nanosheets as a function of temperature and determine the water content, TGA of as-prep γ-Fe_2O_3 was performed (Figure 19) in air. The results show that the TGA curve exhibits a continuous weight loss from room temperture to 500 °C, which can be attributed to the physically and chemically adsorbed water lost in as-prep γ-Fe_2O_3.[114] The TGA shows two mass-loss regions: (i) the first from room temperature to ~400 °C and (ii) from ~400-450 °C, which can attributed to loosely-bound and more strongly bound water respectively. Then after~450 °C, no sharp decrease in weight is observed, which is in the

range of prior work.[115-116] From TGA analysis, the as-prepared γ-Fe_2O_3 nanosheets were determined to be a hydrated phase.

Thermal treatment of as-prep γ-Fe_2O_3 can lead to a phase transition to α-Fe_2O_3 based on the prior work, but its effect on morphology of γ-Fe_2O_3 nanosheets has not been evaluated.[37] In addition, it has been reported that the morphology of iron oxide nanomaterials has a significant impact on its electrochemical properties as an anode for lithium-ion batteries.[97] Thus, the based on the transformation temperatures from TGA, we investigated relatively low temperature treatments (200 °C) along with higher temperatures (350 °C and 450 °C) to determine the effect of temperature treatments on the phase and morphology of γ-Fe_2O_3 nanosheets, and more importantly, the effect of two factors (phase and morphology) on the electrochemical properties of iron oxide nanosheets as cathodes for lithium-ion batteries.

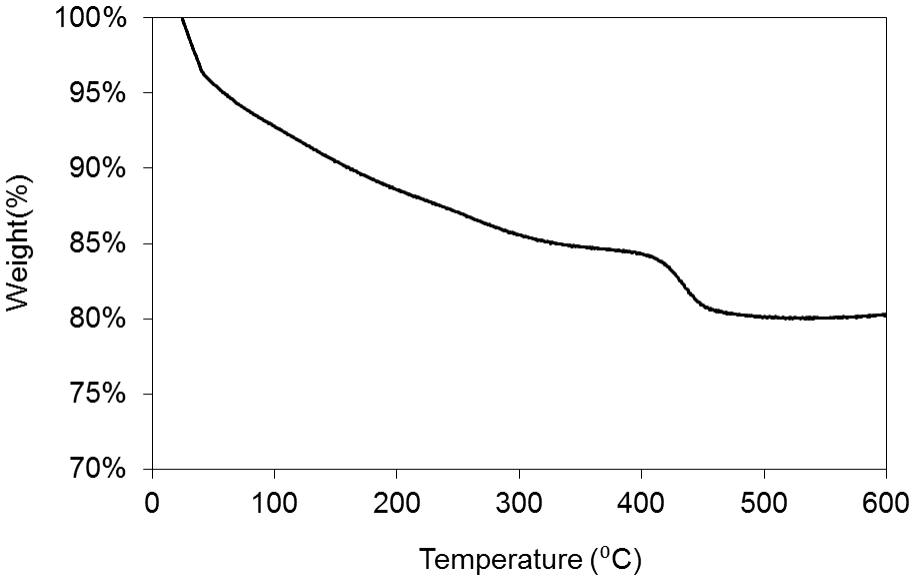

Figure 19. TGA curve of as-prep γ-Fe_2O_3 nanosheets.

3.2.2 XRD of γ-Fe_2O_3 Nanosheets with Different Thermal Treatment

XRD was used to determine the phases of the 200 °C, 350 °C, 450 °C-heated samples and as-prep γ-Fe_2O_3 nanosheets as a comparsion, as shown in Figure 20. The XRD peaks for the 200 °C heated sample show are consistent with either Fe_3O_4 or γ-Fe_2O_3. Compared with the as-prepared γ-Fe_2O_3 nanosheets sample, the 200 °C-heated sample has a peak centered at 2θ=35.512°, which is broader and slightly shifted compared with the as-prepared sample, 2θ = 35.400°. For the sample treated at 350 °C, the XRD peak and positions were very similar to those present for the sample treated at 200 °C. For 350 °C sample, in addition to peaks that are predominantly consistent with Fe_3O_4 or γ-Fe_2O_3, diffraction of (012) and (104) planes with low relative intensity which are consistent with α-Fe_2O_3, hematite (JCPDS card no.33-0664) were observed.[117] The 450 °C treated sample exhibits peaks that are consistent with α-Fe_2O_3.

According to a prior study, thermal treatment can lead to a phase transition from γ-Fe_2O_3 to α-Fe_2O_3.[37] The annealing process from 25 °C to 300 °C was reported to be mainly responsible for inducing important defects at the surface of maghemite.[37] Changes from 300-400°C are mainly related to the generation of the hematite phase, which is consistent with the obtained XRD data. As the temperature increases, the heat facilitates the movement of the atoms and diffusion of Fe^{3+} cations. Furthermore, during the range from 400 °C to 500 °C, hematite has gradually formed and crystallized, which explains the complete disappearance of the maghemite peaks when the annealing temperature is 450 °C.[37]

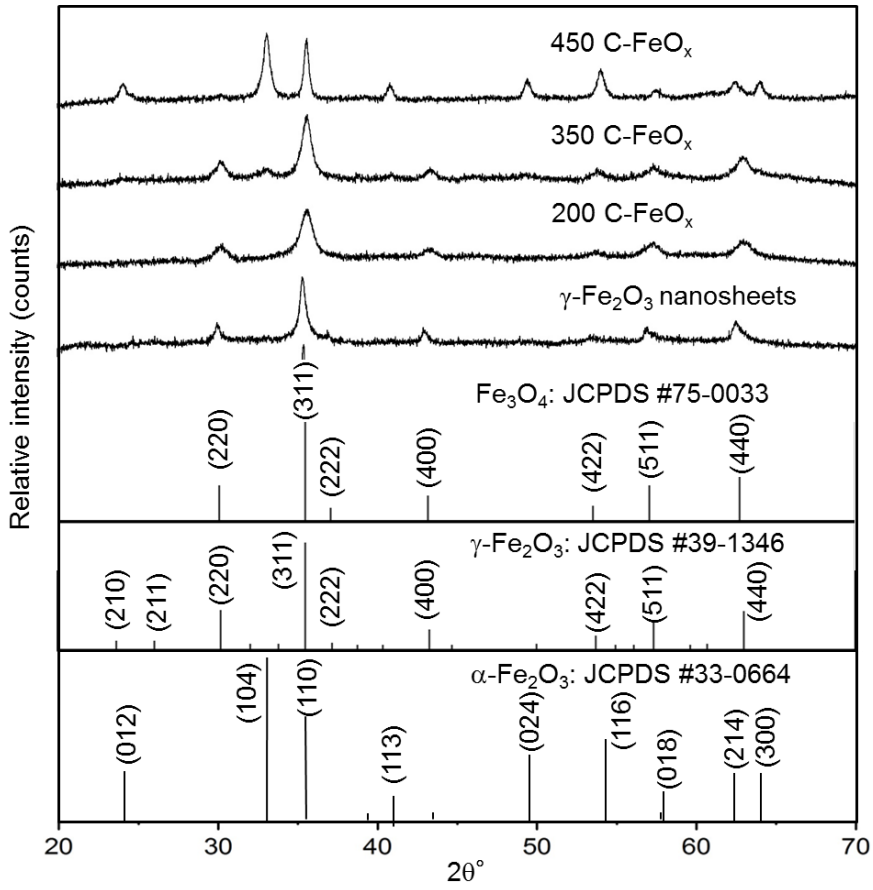

Figure 20. Comparison of XRD data of γ-Fe_2O_3 nanosheets with or without thermal treatment at different temperatures.

The crystallite size of the as-prepared FeO_x nanosheets, 200 °C, 350 °C and 450 °C heated samples(shown in Table 1) was also detected from the Scherrer equation, $L = K\lambda/\beta\cos\theta$, in which L is crystallite size, λ (Å) is wavelength, β is full width at half maximum of peaks in radian located at any 2θ in the pattern, K is a constant related to crystallite shape, normally taken as 0.9. The θ can be in degrees or radians, since the cosθ corresponds to the same number.[118] Analysis of the crystallite size (Table 1) from XRD peak widths shows that for the as prep FeO_x nanosheets, the crystallite size is 10.8 nm. The crystallite size changes from 10.2 nm, 9.2 nm, 12.9 nm or 23.7 nm for as-prep FeO_x nanosheets, 200 °C, 350 °C and 450 °C heated samples respondingly, which is due to the

heat treatment promoting atomic diffusion and leading to an increase in nanoparticle size. Noticeably, the shape factor, *K*, taken as 0.9, is usually used for calculating the crystallite sizes of nanoparticles, but does not accurately represent the size of nanosheets.

Table 1. Crystallite size of FeO_x samples based on analysis of XRD and calculation using Scherrer equation.

Sample	Crystallite Size (nm)
FeO_x-EG-as prep	10.9
FeOx-EG-200	9.2
FeOx-EG-350	12.9
FeOx-EG-450	23.7

3.2.3 Raman spectroscopy of FeO_x Nanosheets with Different Thermal Treatment

In addition to XRD, Raman spectroscopy was used to probe the effect of temperature treatments on the local structure. As shown in Figure 21, the Raman spectrum of the sample heated to 200 °C (200C-FeO_x) is consistent with the local structure of γ-Fe_2O_3. In contrast, the sample heated to 350 °C (350C-FeO_x) shows significantly different Raman bands than the sample heated to 200 °C. The bands for the 350C-FeO_x sample are similar to α-Fe_2O_3 indicating that further heating results in the transformation of the local structure from maghemite, γ-Fe_2O_3, to hematite, α-Fe_2O_3. In addition, it has been reported that transmission Mössbauer spectrometry has been performed to detect the presence of α-Fe_2O_3 phases when γ-Fe_2O_3 is annealed at 350 °C.[37] Heating to 450 °C (450C-FeO_x) results in Raman bands that are consistent with α-Fe_2O_3.[119] Both XRD and Raman spectroscopy characterization show the same transition from the γ-Fe_2O_3 to α-Fe_2O_3 under the thermal treatment.

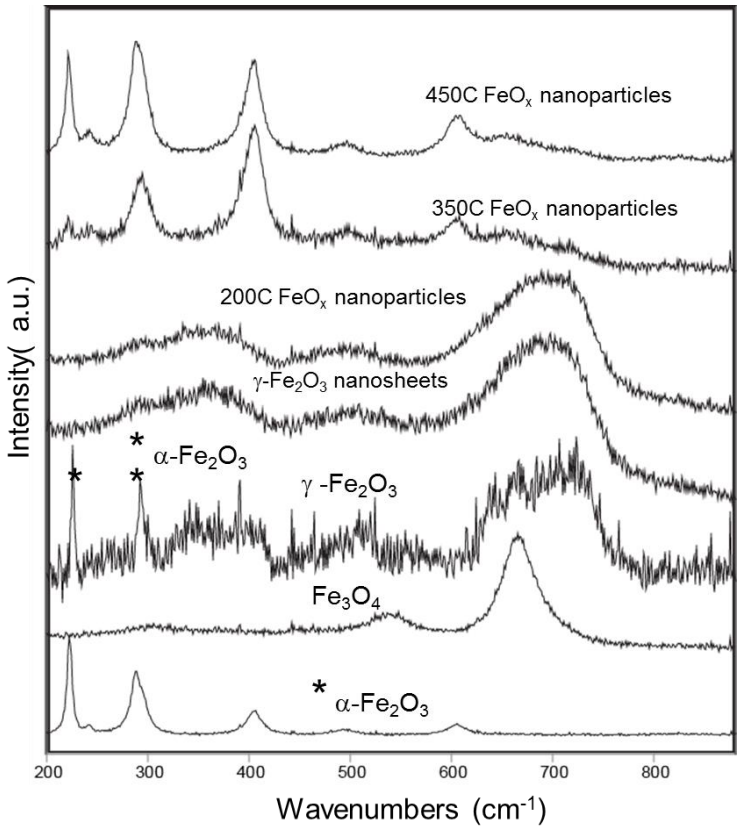

Figure 21. Comparison of Raman spectra of iron oxide samples in the 200-900 cm^{-1} spectra region of γ-Fe_2O_3 nanosheets with or without thermal treatment at different temperatures.

3.2.4 TEM and SEM of FeO_x Nanosheets with Different Thermal Treatment

After determination of the effect of different temperatures on the structure of γ-Fe_2O_3 nanosheets via XRD and Raman spectroscopy, the TEM and SEM were used to characterize the morphology of the heated samples (200 °C, 350 °C and 450 °C). Shown in Figure 22 are representative TEM images of as-prepared γ-Fe_2O_3 and heated samples (200 °C, 350 °C and 450 °C) synthesized using a EG:water solution. From analysis of the TEM images for the as-prepared sample, the nanosheets have approximate lateral dimensions of ~60 nm and thicknesses of ~1 nm. According to the XRD data, the

crystallite size is 10.8 nm, which demonstrates that the γ-Fe_2O_3 nanosheets are polycrystalline.

Furthermore, the TEM results show that the samples heated to 200 °C, 350 °C and 450 °C transform into nanoparticles/nanoplates. From the TEM images, the approximate sizes of nanoparticles/nanoplates are 5.5, 14.5 and 18.7 nm for the 200 °C, 350 °C and 450 °C treated samples respectively, which are similar to calculated sizes from the XRD data. The dimensions of the nanoparticles/nanoplates are significantly smaller than the dimensions of the as-prepared nanosheets. The 200 °C sample showed primarily nanoparticles/nanoplates, however a small number of nanosheets were observed within the TEM images indicating a partial transformation to nanoparticles at 200 °C. At higher temperatures of 350 °C and 450 °C, only nanoparticles were observed. The size of the nanoparticles for the 450 °C-treated sample is larger than the size of the nanoparticles for the 350 °C-treated sample, which supports the growth of nanoparticles occurs at higher temperatures.

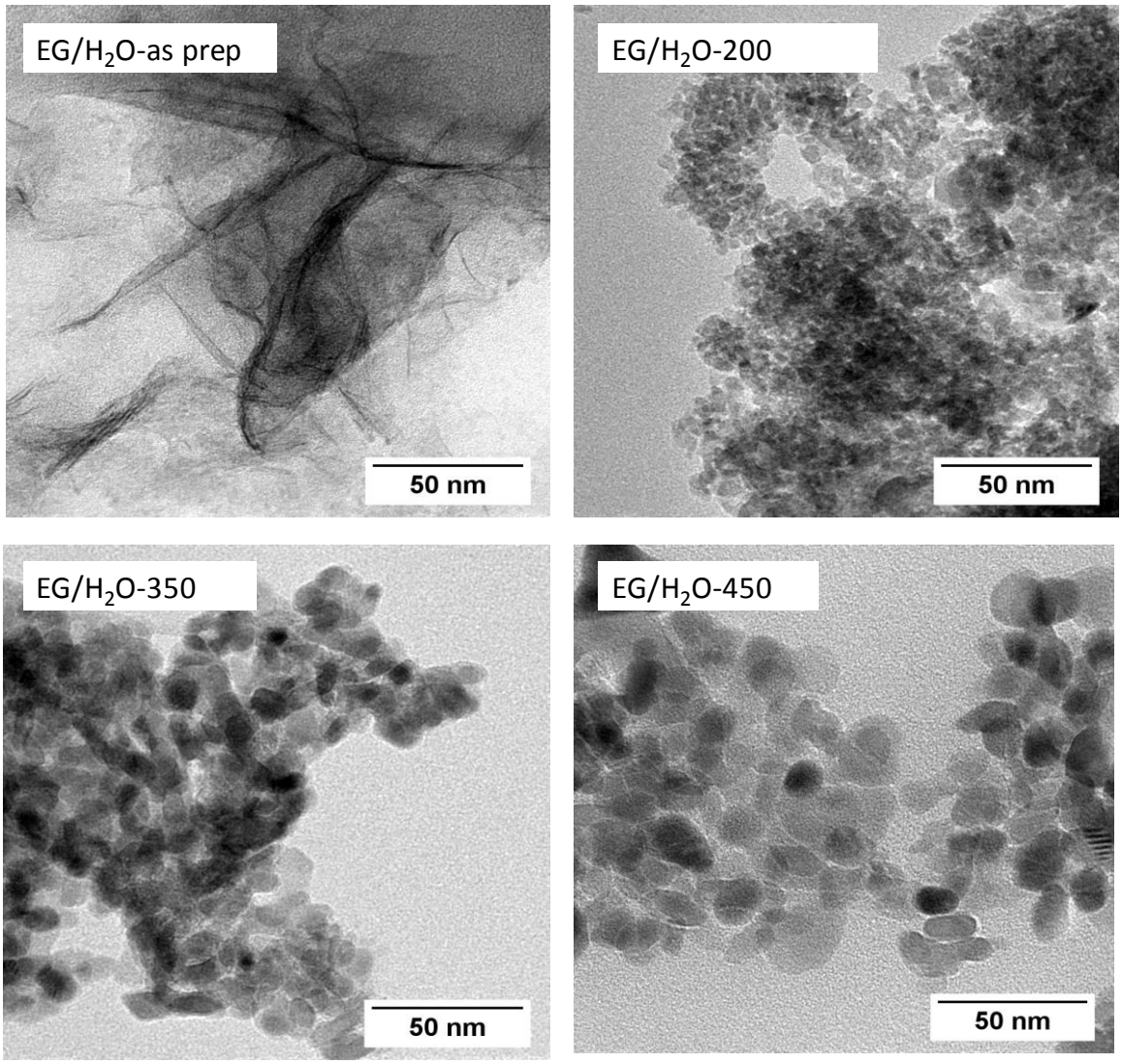

Figure 22. TEM images of γ-Fe_2O_3 nanosheets treated at different temperatures, and γ-Fe_2O_3 nanosheets as a comparison.

Similar to TEM, the scanning electron microscope (SEM) is another technique to characterize the morphology of nanoparticles. Compared with TEM, SEM uses a focused beam of high-energy electrons to generate a variety of signals at the surface of solid specimens, whereas TEM uses a beam of electrons which transmit through an ultra-thin specimen, interacting with the specimen as it passes through it. Scanning electron microscopy (SEM) images of as-prepared γ-Fe_2O_3 and heated samples (200 °C, 350 °C

and 450 °C) synthesized using a EG:water solution are shown in Figure 23. The SEM images further show that the as-prep FeO_x consists of nanosheets and when the temperature increased from 200 °C to 450 °C, the FeO_x nanosheets transform into nanoparticles.

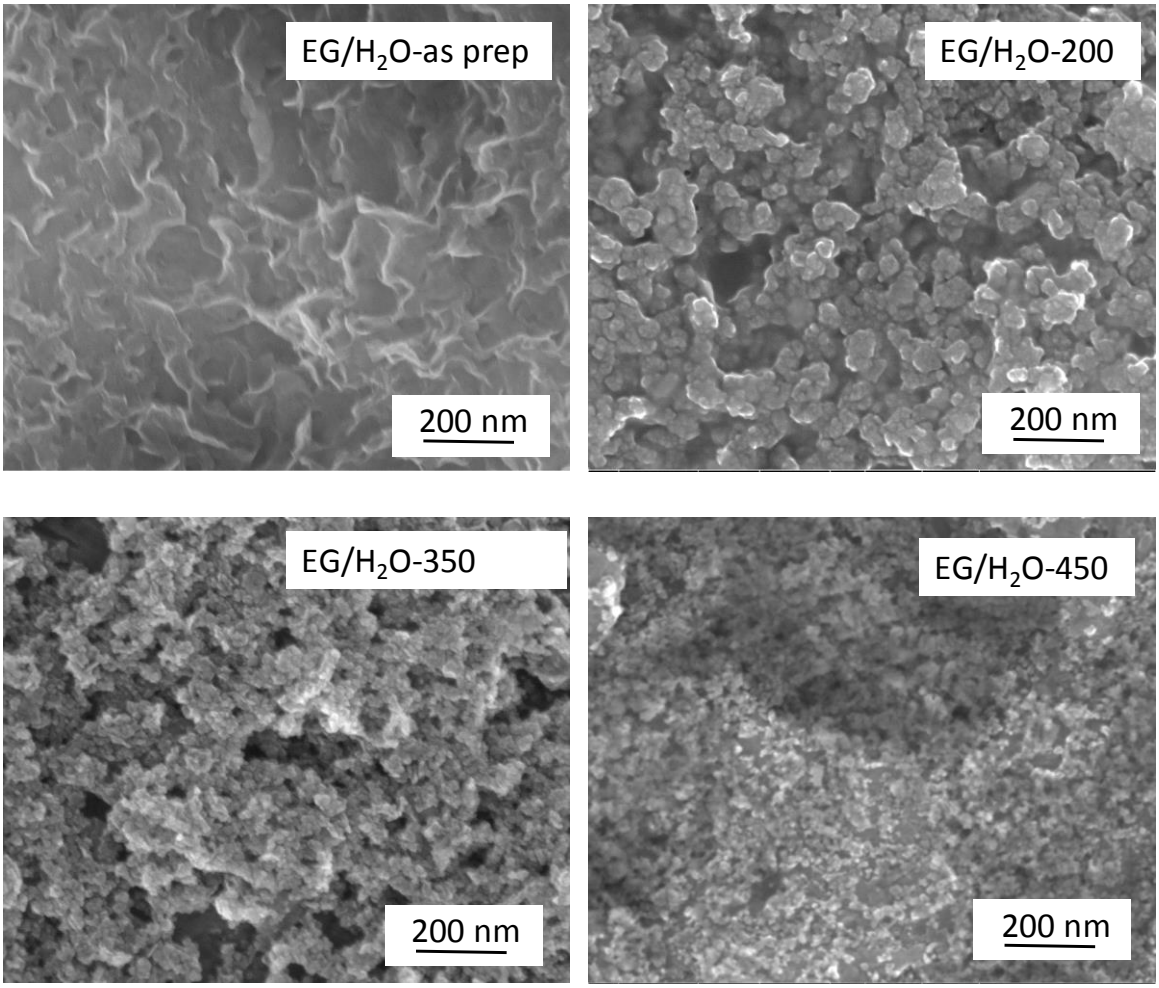

Figure 23. SEM images of γ-Fe_2O_3 nanosheets treated at different temperatures, and γ-Fe_2O_3 nanosheets as a comparison.

3.2.5 Microscopy Analysis of As-prep γ-Fe_2O_3 Nanosheets with Mild Heat Treatment

From the TEM and SEM images above, it is clear that the morphology of nanosheets is sensitive to heat treatment. The as-prep γ-Fe_2O_3 nanosheets require mild heat treatment for making the electrode (dried in a vacuum oven at 120 °C for 16 h). Therefore, the morphology of as prep γ-Fe_2O_3 sample treated at 120°C under vacuum was determined. Figure 24 (a) and (b) shows the TEM and SEM images of the as-prepared γ-Fe_2O_3 nanosheets with mild treatment (EG/H_2O-120v) respectively. From the analysis of the TEM and SEM images, after low temperature and vacuum treatment, the sample keeps the nanosheet structure. Furthermore, the results of Raman analysis shows that the sample with mild thermal treatment is still γ-Fe_2O_3 phase, as shown in Figure 25. Therefore, the samples tested in coin cells retains the γ-Fe_2O_3 nanosheet structures.

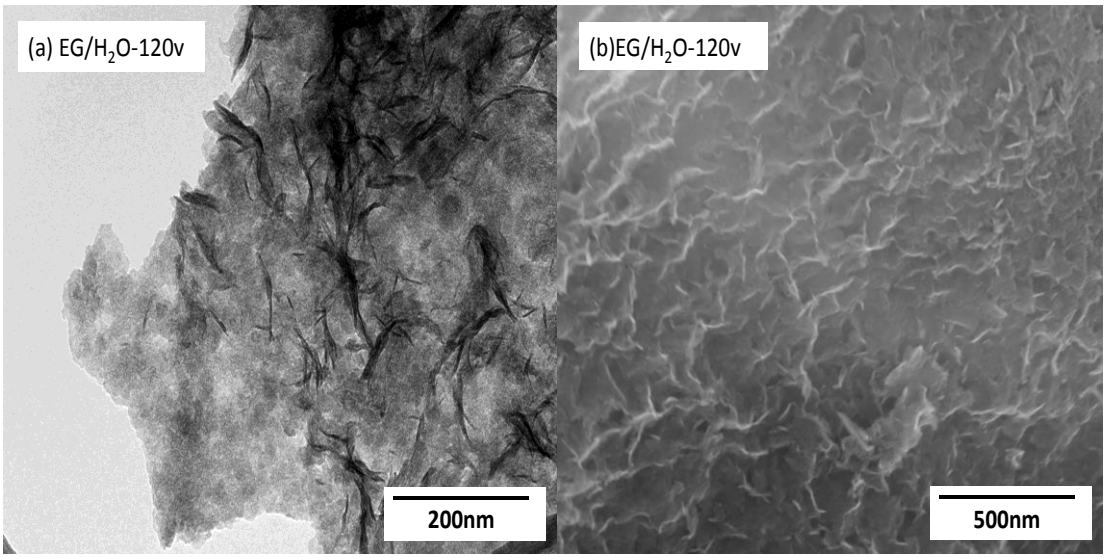

Figure 24. (a) TEM image and (b) SEM image of FeO_x nanosheets with mild treatment.

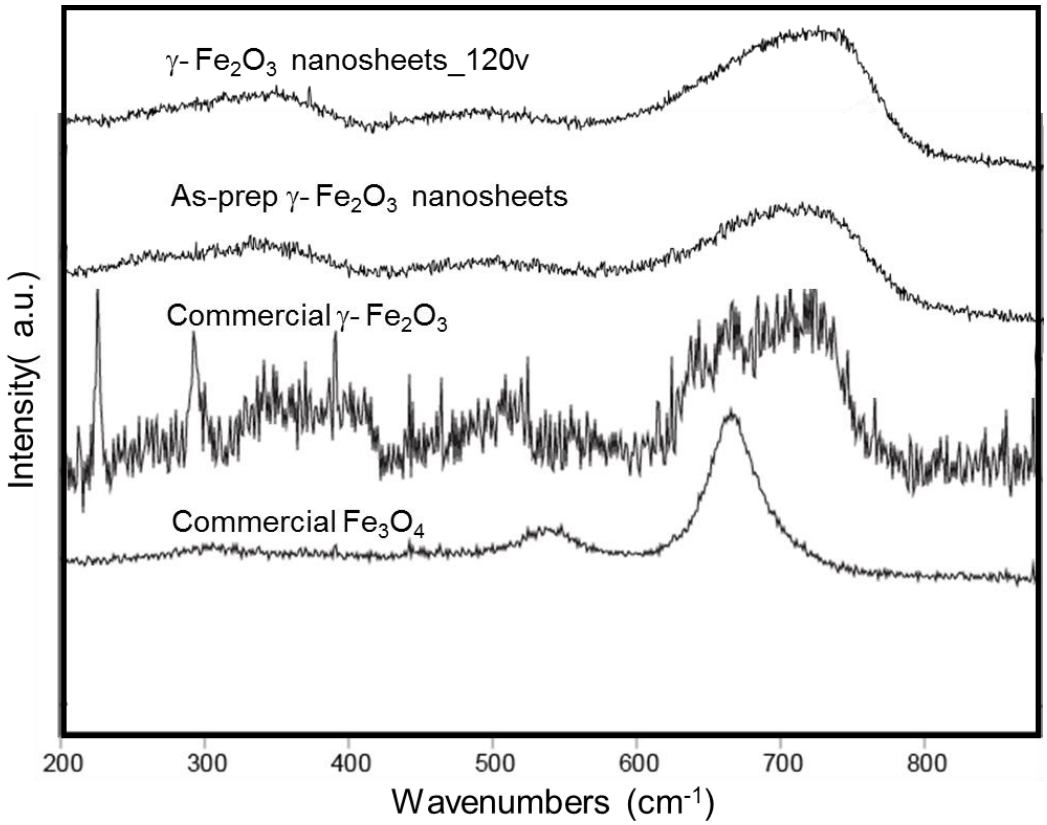

Figure 25. Comparison of Raman spectra of iron oxide samples in the 200-900 cm^{-1} spectra region of γ-Fe_2O_3 nanosheets with or without thermal temperatures and referenced samples.

3.3 The Electrochemical Properties of γ-Fe_2O_3 Nanosheets and FeO_x Nanoparticles

3.3.1 Galvanostatic Charge–discharge of γ-Fe_2O_3 Nanosheets and FeO_x Nanoparticles

Galvanostatic charge–discharge tests were conducted to determine Li-ion charge storage capability. The discharge/charge profiles of γ-Fe_2O_3 nanosheets during the first, second and tenth cycles are shown in Figure 26, which were obtained at a constant mass-nominated current of 3 mA g^{-1} within a potential range of 1.5–4.2V vs Li. During the first cycle, the discharge capacity of γ-Fe_2O_3 nanosheets was 190 mAh g^{-1}, however, FeO_x nanosheets have the second cycle reversible capacity of 146 mAh g^{-1}. This irreversible

capacity loss in the second cycle can be attributed to either the formation of a solid electrolyte interphase.[97, 120] or a structural transformation. After ten cycles, the discharge capacity was 140 mAh g^{-1}.

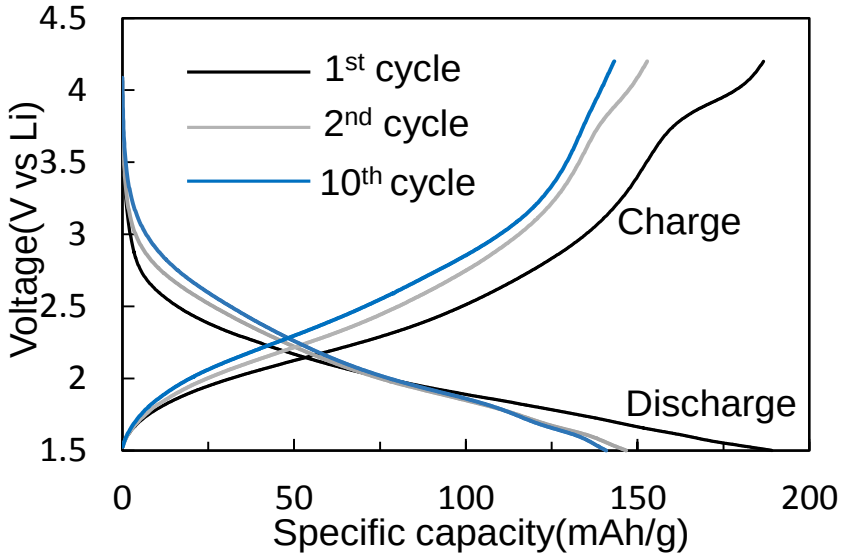

Figure 26. Discharge/charge profiles of the γ-Fe_2O_3 nanosheets at current of 3 mA/g. 1.0 M $LiPF_6$ in EC: DEC (1:1), Ref/ Counter: Li

The discharge/charge profiles for the second cycle of γ-Fe_2O_3 nanosheets, heated samples (200 °C, 350 °C and 450 °C) and commercial γ-Fe_2O_3 nanoparticles are compared in Figure 27, at mass-nominated current of 3 mA g^{-1} within 1.5–4.2V. The γ-Fe_2O_3 nanosheets exhibited significantly higher discharge capacities compared to all the FeO_x nanoparticles which showed specific discharge capacities of 100, 82, 58 and 32 mAh g^{-1} for the 200 °C, 350 °C, 450 °C-treated samples and commercial γ-Fe_2O_3 nanoparticles respectively. The γ-Fe_2O_3 nanosheets also show higher capacity compared to prior work.[47, 121] In addition, higher temperature treatments resulted in decreased capacities of FeO_x nanoparticles compared with samples treated at lower temperatures.

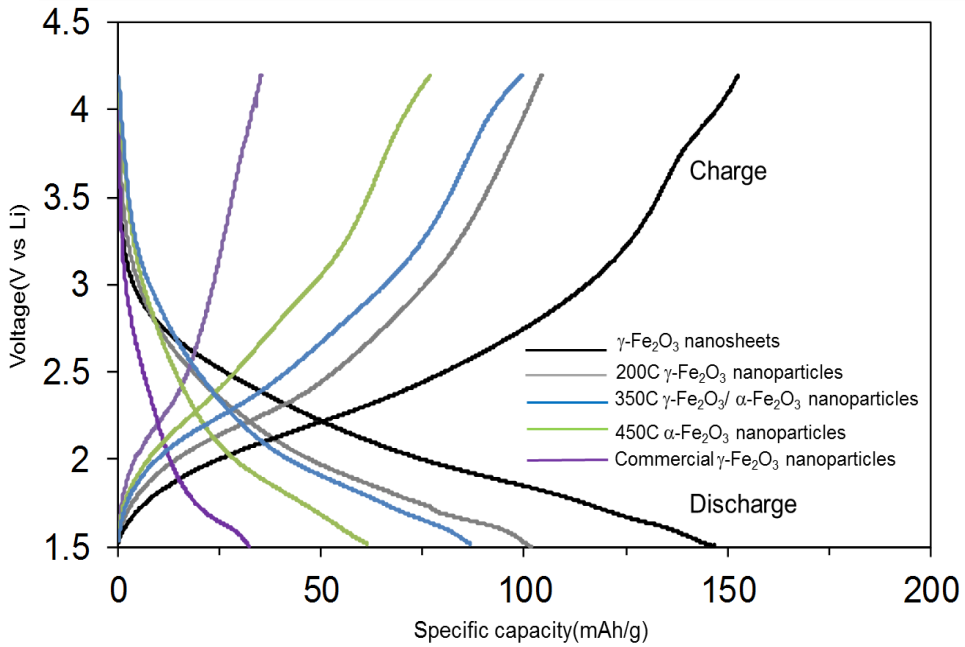

Figure 27. Comparison of discharge/charge profiles of the γ-Fe_2O_3 nanosheets and FeO_x nanoparticles at current of 3mA g^{-1}. 1.0 M $LiPF_6$ in EC: DEC (1:1), Ref/ Counter: Li

The γ-Fe_2O_3 nanosheets enabled the storage of 0.9 moles Li per mole Fe_2O_3 ($Li_{0.9}Fe_2O_3$) which was significantly higher than that of γ-Fe_2O_3 and α-Fe_2O_3 nanoparticles (Table 2).

Table 2. Amount of Li^+ ions storage in γ-Fe_2O_3 nanosheets and FeO_x nanoparticles at current of 3 mA g^{-1}.

Sample	Moles of Li^+ per mole Fe_2O_3
γ-Fe_2O_3 nanosheets	0.9
200C γ-Fe_2O_3 nanoparticles	0.6
350C γ-Fe_2O_3/ α-Fe_2O_3 nanoparticles	0.4
450C α-Fe_2O_3 nanoparticles	0.3
Commercial γ-Fe_2O_3	0.2

3.3.2 Comparison of Rate Capability of γ-Fe_2O_3 nanosheets and FeO_x Nanoparticles

To further investigate the electrochemical performance of the γ-Fe_2O_3 nanosheets and Fe_2O_3 nanoparticles, the rate capabilities were tested as shown in Table 3. γ-Fe_2O_3 nanosheets exhibits a much better rate performance at different mass-nominated current, 3 mA g^{-1}, 30 mA g^{-1}, 60 mA g^{-1}, 150 mA g^{-1} and 300 mA g^{-1}. Specifically, at a current of 30 mA g^{-1}, nanosheets provided much higher discharge capacities, 142 mAh g^{-1}, compared to 94, 84, and 54 mAh g^{-1} for the 200 °C, 350 °C and 450 °C-treated samples respectively. However, as the rate increases, the difference in discharge capacities between γ-Fe_2O_3 nanosheets and nanoparticles becomes smaller because of lower capacities at high current. In addition, it is shown that there is not a significant difference between the discharge capacity of 200 °C and 350 °C FeO_x nanoparticles, whereas the discharge capacity of 450 °C FeO_x nanoparticles exhibit a much lower discharge capacity compared to that of 200 °C sample. That is probably because the 450 °C FeO_x sample is completely transformed into α-Fe_2O_3, however, 350 °C FeO_x sample is in the transition of γ-Fe_2O_3, which has cation defect structure can significantly enhance the lithium-ion storage compared to α-Fe_2O_3.[122] Noticeably, shown in Figure 28, even at high rates - corresponding to an average discharge time of 17 minutes (3.6 C-rate), the iron oxide nanosheets showed a capacity of 82 mAh g^{-1} which was higher than that of all other tested nanoparticles. The capacity of a battery is commonly rated at 1C, which represents the full charge or discharge of a battery or an electrode material in 1 hour.

Table 3. Electrochemical properties of iron oxide nanomaterials; average discharge capacity (mAh g^{-1}) from the 2nd cycle at different mass normalized currents of 3, 30, 60, 150 and 300 mA g^{-1}.

Material ID	Average discharge capacity (mAh g^{-1}) at mass normalized current				
	3 mA g^{-1}	30 mA g^{-1}	60 mA g^{-1}	150 mA g^{-1}	300 mA g^{-1}
γ-Fe_2O_3 nanosheets	147.6	136.7	120.9	102.0	82.2
200C γ-Fe_2O_3 nanoparticles	100.2	90.6	80.3	73.6	64.8
350C γ-Fe_2O_3/ α-Fe_2O_3 nanoparticles	83.1	80.9	70.4	52.9	46.2
450C α-Fe_2O_3 nanoparticles	66.2	53.3	46.3	43.0	40.4
Commercial γ-Fe_2O_3 nanoparticles	32.1	30.4	27.8	24.3	19.2

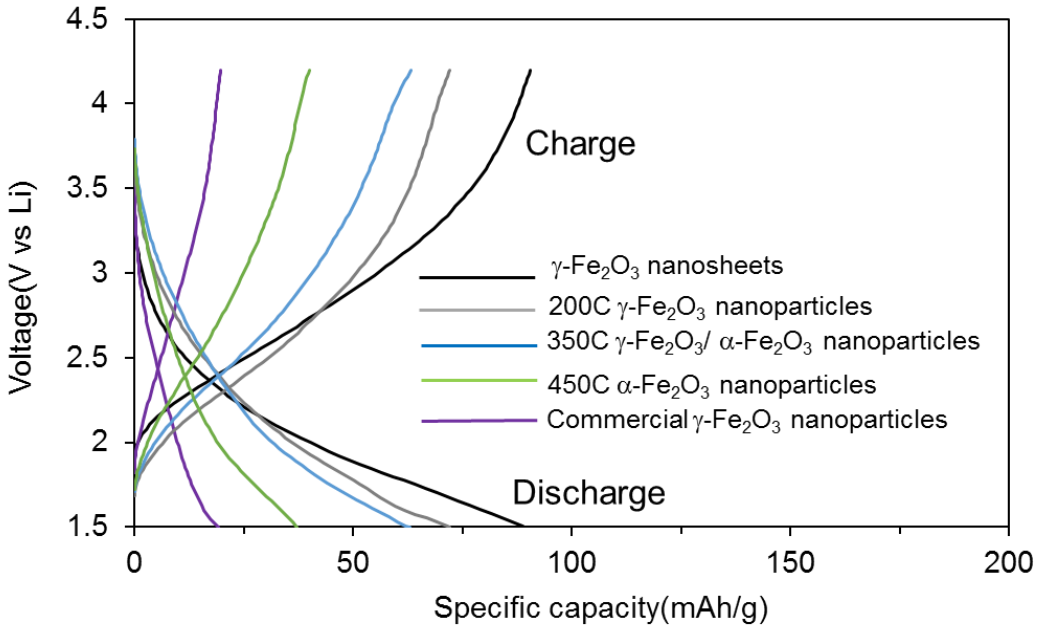

Figure 28. Comparison of discharge/charge profiles of the γ-Fe_2O_3 nanosheets and FeO_x nanoparticles at current of 300 mA g^{-1}. 1.0 M $LiPF_6$ in EC: DEC (1:1), Ref/ Counter: Li

3.3.3 Comparison of Cycling Performance of γ-Fe_2O_3 Nanosheets and FeO_x Nanoparticles

Cycling tests were performed to determine the reversibility of Li-ion charge storage. In addition to higher specific discharge capacities and improved rate capabilities, the γ-Fe_2O_3 nanosheets exhibited a high capacity retention of 86.0% of initial capacity after 40 cycles (2^{nd} cycle to 40^{th} cycle) as shown in Figure 29 and Table 4. Figure 28 compares the cycling performances of the FeO_x nanosheets and 200 °C, 350 °C, 450 °C-treated and commercial γ-Fe_2O_3 nanoparticles samples at a mass normalized current of 30 mA g^{-1}. γ-Fe_2O_3 nanosheets display a continuously high discharge capacity after 40 cycles, which is 1.5 times and 2.6 times as large as that of 200 °C and 450 °C FeO_x nanoparticles respectively. In addition, γ-Fe_2O_3 nanosheets and 200 °C, 350 °C,

450 °C-treated and commercial γ-Fe_2O_3 nanoparticles samples have similar capacity retention and coulombic efficiency (Table 3). The 200 °C and 350 °C treated sample show a higher capacity retention of 87 % and 91 % respectively than that of γ-Fe_2O_3 nanosheets, however this is attributed to its relatively low initial capacity.

Table 4. Summary of cycling performance of γ-Fe_2O_3 nanosheets as well as FeO_x nanoparticles at current of 30 mA g^{-1}.

Sample Notation	Capacity Retention after 2^{nd} to 40^{th} cycle (%)	Coulombic efficiency (%),2-40^{th} cycle
γ-Fe_2O_3 nanosheets	88.0	98.2
200C γ-Fe_2O_3 nanoparticles	86.7	99.2
350C γ-Fe_2O_3/ α-Fe_2O_3 nanoparticles	90.9	99.2
450C α-Fe_2O_3 nanoparticles	82.6	98.6
Commercial γ-Fe_2O_3 nanoparticles	86.6	99.4

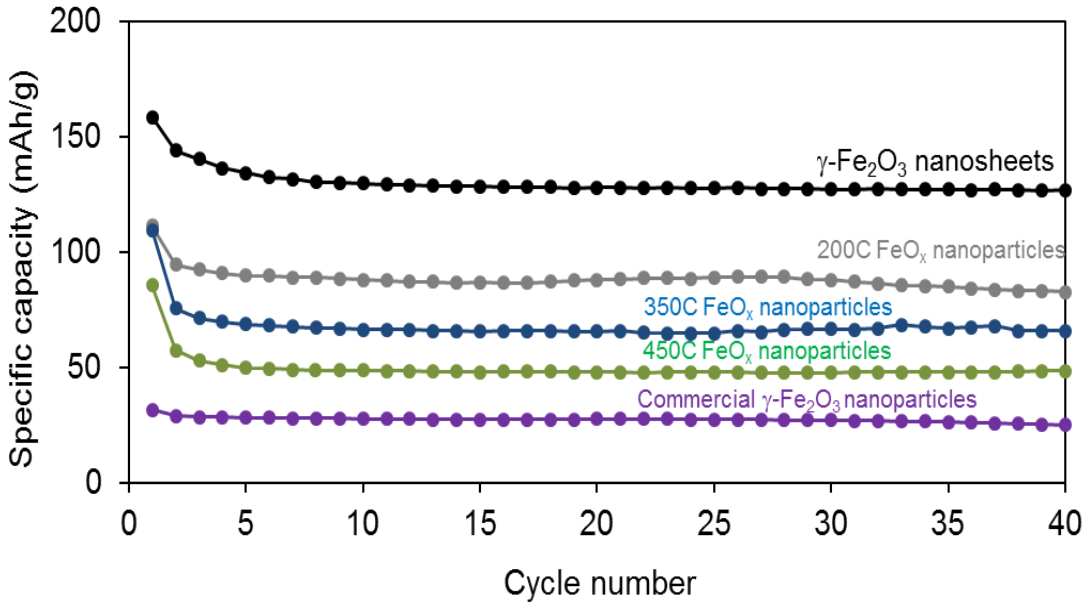

Figure 29. Capacity retention upon cycling for γ-Fe_2O_3 nanosheets compared with FeO_x nanoparticles; electrolyte: 1 M $LiPF_6$ in EC: DEC; 1:1 v/v; counter/reference: metallic Li; voltage range of 1.5-4.2 V vs Li; mass-normalized current of 30 mA g^{-1}.

3.4 Factors that Contribute to Improved Electrochemical Properties of γ-Fe_2O_3 Nanosheets

3.4.1 Surface Area of γ-Fe_2O_3 Nanosheets and FeO_x Nanoparticles

The specific surface area of a powder can be measured by physical adsorption of a gas on the surface of material and by calculating the amount of adsorbate gas corresponding to a monomolecular layer on the surface. Physical adsorption results from relatively weak forces (van der Waals forces) between the adsorbate gas molecules and the adsorbent surface area of the test powder. To explore the specific surface area of γ-Fe_2O_3 nanosheets and 200 °C, 350 °C, 450 °C-treated samples, nitrogen sorption experiments were carried out. Figure 30 shows the adsorption–desorption isotherm plots

of γ-Fe_2O_3 nanosheets and heat treated samples, all of which exhibit a type II characteristic hysteresis loop, indicating that there are mesopores in the samples.[97, 123] The Brunauer–Emmett–Teller (BET) surface areas of all the samples are shown in Table 5. The surface area of γ-Fe_2O_3 nanosheets is 138 m^2 g^{-1}, which is much higher than that of 200 °C, 350 °C and 450 °C FeO_x nanoparticle samples. As the thermal treatment temperatures increased, the surface areas decreased correspondingly. Prior work showed that 2D α-Fe_2O_3 nanomaterials usually exhibit larger surface area than that of nanoparticles, which is closely related with enhanced capability of the Li ion storage and faster Li ion diffusion as anodes for lithium-ion batteries.[124] Therefore, larger surface area could be one of factors that contributes to improved electrochemical properties of γ-Fe_2O_3 nanosheets.

Table 5. Summary of BET surface area of γ-Fe_2O_3 nanosheets as well as the FeO_x nanoparticles.

Sample	BET surface area (m^2 g^{-1})
γ-Fe_2O_3 nanosheets	138.9 ±8.9
200C γ-Fe_2O_3 nanoparticles	98.5±3.5
350C γ-Fe_2O_3/ α-Fe_2O_3 nanoparticles	70.1±0.0
450C α-Fe_2O_3 nanoparticles	43.0 ±0.8

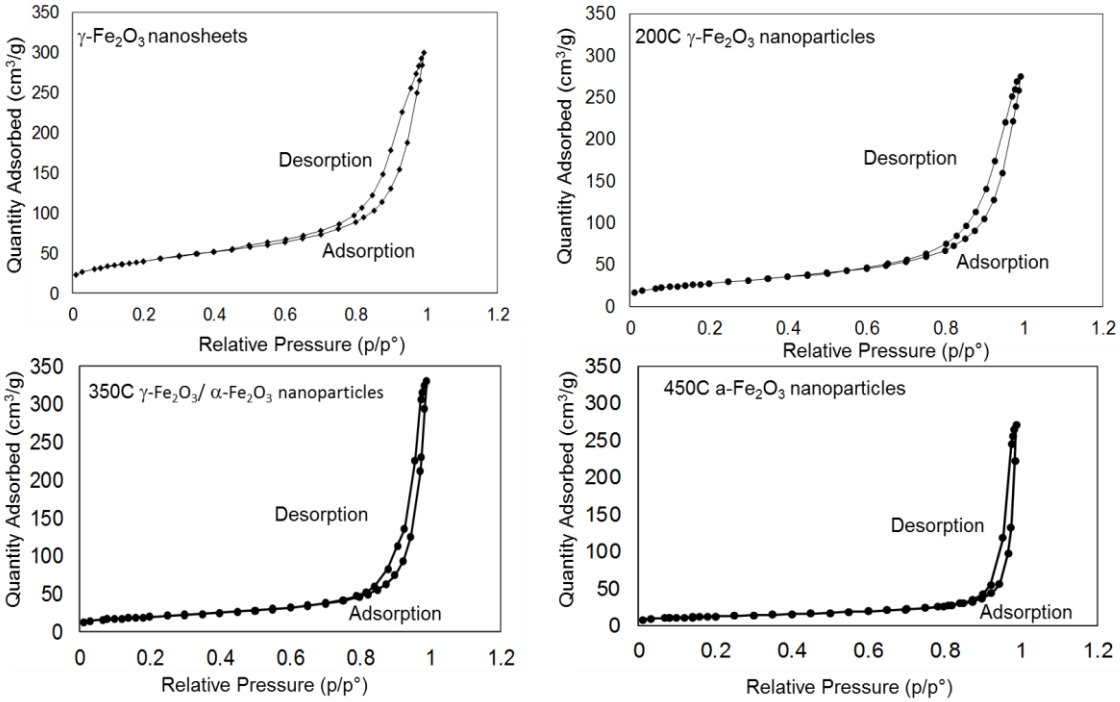

Figure 30. Nitrogen sorption isotherms of γ-Fe_2O_3 nanosheets as well as the FeO_x nanoparticles.

3.4.2 Kinetics of the γ-Fe_2O_3 Nanosheets and Nanoparticles

The kinetics of the Li-ion charge storage within γ-Fe_2O_3 nanosheets, 200C γ-Fe_2O_3 nanoparticles and commercial γ-Fe_2O_3 nanoparticles were also investigated by performing cyclic voltammograms using different scan rates (0.1, 0.5, 1, 5, 10 mV/s) to evaluate the difference of charge storage process (diffusion and capacitive) between nanosheets and nanoparticles. Prior work shows that charge storage kinetics can be probed by analysis of cyclic voltammograms (CVs) with different scan rates.[125]

Figure 31 shows the comparison of CV response of γ-Fe_2O_3 nanosheets, 200C γ-Fe_2O_3 nanoparticles and commercial γ-Fe_2O_3 nanoparticles at scan rate of 0.5 mV s^{-1}. For γ-Fe_2O_3 nanosheets, the CV exhibits two peaks, one dominated peak is at ~2.3 V (vs.

Li/Li$^+$) and the other weak peak is at ~2.9 V (vs. Li/Li$^+$) for the positive scan. For the negative scan, the γ-Fe_2O_3 nanosheets have a peak ~1.7 V (vs. Li/Li$^+$). The potentials observed in the CV of γ-Fe_2O_3 nanosheets are consistent with the voltage profiles from the galvanostatic tests. In the CV, the γ-Fe_2O_3 nanosheets exhibit dramatically higher mass-normalized currents compared to the γ-Fe_2O_3 nanoparticles indicating that more charge can be stored within the nanosheet architecture for the same mass of material.

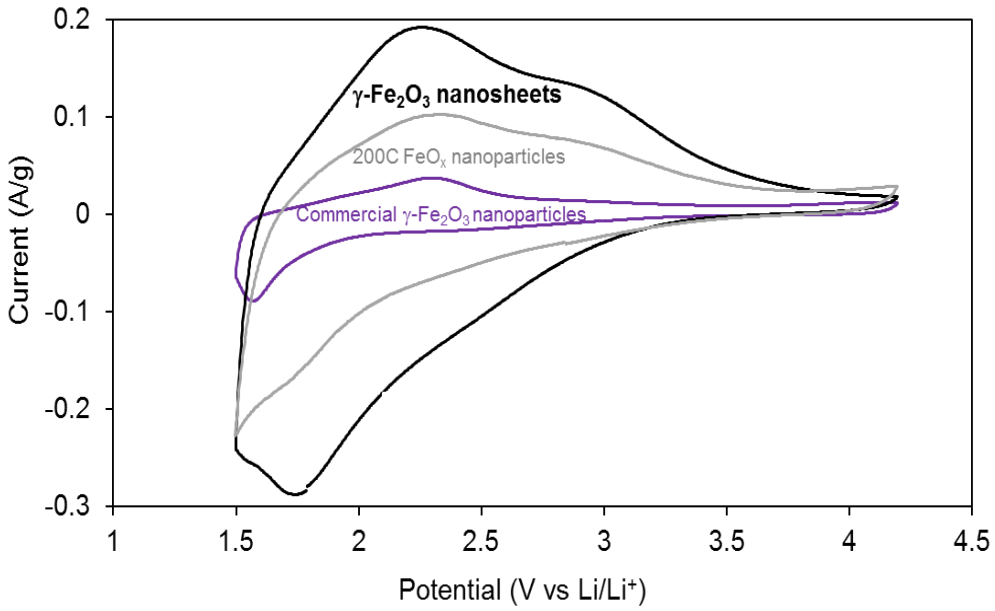

Figure 31. Cyclic voltammograms (CVs) of γ-Fe_2O_3 nanosheets compared with 200C γ-Fe_2O_3 nanoparticles and commercial γ-Fe_2O_3 nanoparticles. scan rate 0.5 mV/s; electrolyte: 1 M $LiPF_6$ in EC: DEC; 1:1 v/v; counter/reference: metallic Li

CV analysis was carried out to evaluate the electrochemical behavior and kinetic characteristics of γ-Fe_2O_3 nanosheets between 1.5 and 4.2 V, and the cyclic voltammetry for the second cycles with different scan rate (0.1, 0.5, 1, 5, 10 mV/s) are shown in the Figure 32. The curve shows one cathodic peak (reduction) located at 1.7 V and one anodic peak(oxidation) located at 2.4V for the 0.1, 0.5, and 1 mV/s scan rate. These

reduction and oxidation peaks are related to the Fe^{2+}/Fe^{3+} redox couples, which are responsible for the gain and loss of electrons, accompanying Li-ion deintercalation/intercalation.[126-127] However, when the scan rate is increased to 5 and 10 mV/s, the cathodic peaks disappeared and anodic peaks shifted to 2.9 V and 3.4 V for 5 and 10 mV/s scan rate, which is probably due to the high resistance with the electrode.

CV analysis of 200C γ-Fe_2O_3 nanoparticles and commercial γ-Fe_2O_3 nanoparticles show similar behavior when increasing scan rates.

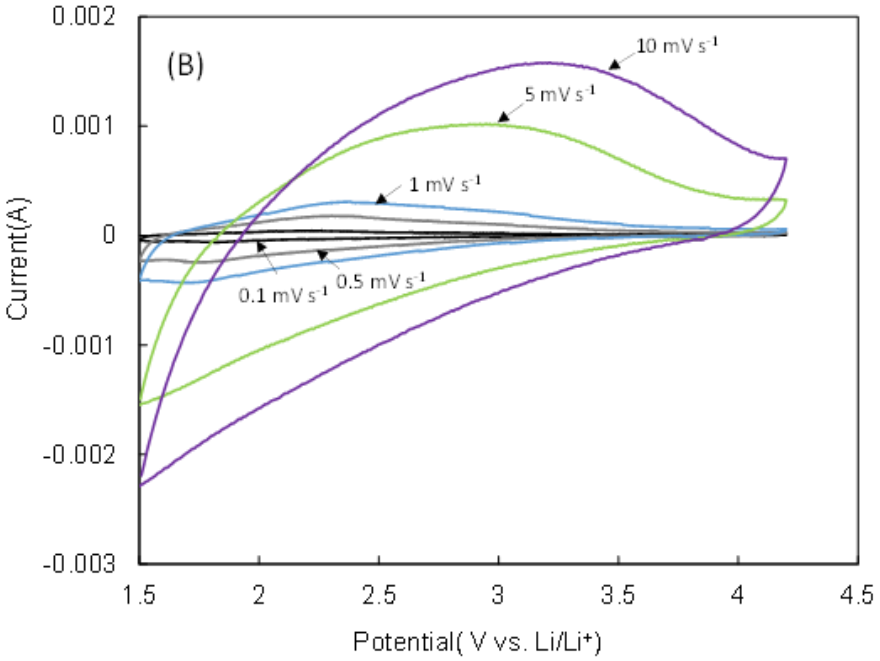

Figure 32. CVs for γ-Fe_2O_3 nanosheets at different scan rates.

According to the prior work, the diffusion and capacitive charge storage process can be determined by performance of the peak current of CV plot (i) vs. scan rate,[128-129] $i = av^b$, where a and b are adjustable values. When the b-value is 1 then the current is capacitive, and when it is 0.5 then it is controlled by semi-infinite diffusion. The b value can be determined by plotting log(i) vs. log(v), which gives the b value through the slope.

In Figure 33, the b-value for the cathodic peak currents in γ-Fe_2O_3 nanosheet is 0.8 from 0.1 to 10 mV/s, which is higher than that of 200C γ-Fe_2O_3 nanoparticles (0.7) and commercial γ-Fe_2O_3 nanoparticles (0.6) respectively, demonstrating most of the current at the peak potential is predominantly capacitive for all the γ-Fe_2O_3 nanomaterial, however, the γ-Fe_2O_3 nanosheets exhibit the most dominant capacitive Li-ion charge storage.

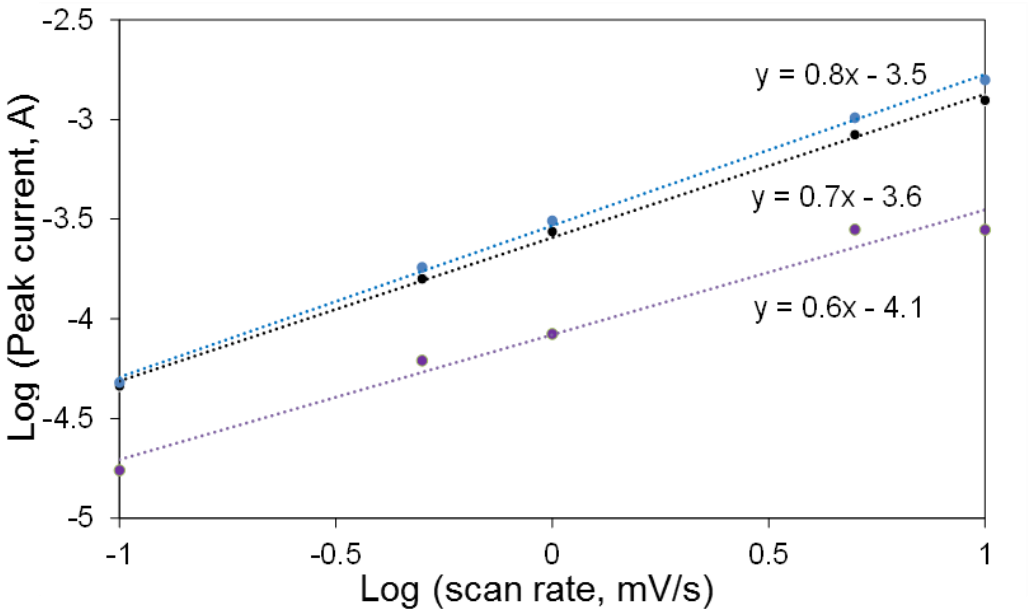

Figure 33. Determination of the b-value of γ-Fe_2O_3 nanosheets, 200C γ-Fe_2O_3 nanoparticles and commercial γ-Fe_2O_3 nanoparticles using the cathodic peak current relationship to sweep rate.

3.4.3 Electronic Conductivity of the γ-Fe_2O_3 Nanosheets and Fe_2O_3 Nanoparticles

Electric conductivity measurement were performed via two-point probe method. The results are shown in Table 6. The as-prep γ-Fe_2O_3 nanosheets show higher electric conductivity than that 200 °C and 350 °C FeO_x nanoparticles. The higher electrical conductivity of nanosheets may be as a result of short distance of electron conducting

path compared with the aggregated nanoparticles or quantum confinement effects.[104] According to the prior study, nanosheet like structure of iron oxides can increase electrochemical performance, especially at high charging and discharging rates.[104]

Table 6. Electronic conductivity of γ-Fe_2O_3 nanosheets and FeO_x nanoparticles.

Sample	σ_{elec} (S/cm)
γ-Fe_2O_3 nanosheets	$2.2\pm 0.4\times10^{-8}$
200C γ-Fe_2O_3 nanoparticles	$7.2\pm 3.5\times10^{-9}$
350C γ-Fe_2O_3/ α-Fe_2O_3 nanoparticles	$7.2\pm 1.1\times10^{-9}$
450C α-Fe_2O_3 nanoparticles	$2.2\pm 0.4\times10^{-8}$

4. CONCLUSIONS

Iron oxide nanomaterials were synthesized via a two-step reaction. The products were characterized by XRD, Raman spectroscopy, TGA, TEM and SEM microscopy and consistent with maghemite (γ-Fe_2O_3) nanosheets. Noticeably, ethylene glycol was observed to be responsible for formation of sheet-like structures, due to its chelating ability.

The γ-Fe_2O_3 nanosheets were annealed at 200 °C, 350 °C and 450 °C in air for 24 hours. The resulting products transformed into nanoparticles with increased sizes with higher temperature treatments. In addtion, the thermal treatment converts the γ-Fe_2O_3 nanosheets completely to α-Fe_2O_3 phase at 450 °C but maintains the γ-Fe_2O_3 phase at 200 °C. The 350 °C treated FeO_x sample shows a mixture of γ-Fe_2O_3 and α-Fe_2O_3 phases.

The electrochemical analysis showed that γ-Fe_2O_3 nanosheets have much higher capacity, better rate capability, and cycling stability than that of 200 °C, 350 °C and 450 °C treated FeO_x nanoparticles as cathodes for lithium-ion batteries. As the annealing temperature increased, the discharge capacity decreased for 200 °C, 350 °C and 450 °C treated FeO_x nanoparticles. Importantly, by comparison to the capacity of current commerical cathodes, such $LiCoO_2$, $LiFePO_4$ and NMC (~140mAh/g), the γ-Fe_2O_3 nanosheets cathodes even exhibit simliar capacity(~140mAh/g) at low current. The improved electrochemical performance of γ-Fe_2O_3 nanosheets is attributed to multiple factors, including (*i*) cationic vacancies, (*ii*) larger surface area, (*iii*) capacitive charge storage, and (*iv*) higher electronic conductivity.

Further studies are needed to improve these materials for battery use. One of the challenges of FeO_x materials as cathodes in lithium-ion batteries is their poor electronic

challenges of FeO_x materials as cathodes in lithium-ion batteries is their poor electronic conductivity that could limit further commercialization. Development of FeO_x nanosheets and graphene nanocomposites could improve the overall electric conductivity and structural stability. Additional studies to understand the fundamental role of ethylene glycol in formation of FeO_x nanosheets would be useful.

LITERATURE CITED

1. Armand, M.; Tarascon, J. M. Building better batteries. *Nature.* **2008**, 451, 652-657.
2. Poizot, P.; Laruelle, S.; Grugeon, S.; Dupont, L. and Tarascon, J. M. Nano-sized transition-metal oxides as negative-electrode materials for lithium-ion batteries. *Nature* **2000**, 407, 496-499.
3. Aricò, A. S.; Bruce. P.; Scrosati, B.; Tarascon, J. M.; Schalkwijk, W. materials for advanced energy conversion and storage devices. *Nat. Mater.* **2005**, 4, 366-377.
4. Dunn, B.; Kamath, H.; Tarascon, J. M. Electrical energy storage for the grid a battery of choices. *Science* **2011**, 334, 928-935.
5. Diouf, B.; Pode, R. Potential of lithium-ion batteries in renewable energy. *Renewable Energy.* **2015**, 76, 375-380.
6. Yang, P.; Tarascon, J. M. Towards systems materials engineering. *Nat. Mater.* **2012**, 11, 560-563.
7. Propfe, B.; Kreyenberg, D.; Wind, J.; Schmid, S. Market penetration analysis of electric vehicles in the German passenger car market towards 2030. *Int. J. Hydrogen Energy.* **2013**, 38, 5201-5208.
8. Goodenough, J. B.; Park, K. S. The Li-ion rechargeable battery: a perspective. *J. Am. Chem. Soc.* **2013**, 135, 1167-1176.
9. Deng, D. Li-ion batteries: basics, progress, and challenges. *Energy Science & Engineering* **2015**, 3, 385-418.

10. Roy, P. S. Nanostructured anode materials for lithium ion batteries. *J. Mater. Chem. A* **2015**, *3*, 2454-2484.

11. Fergus, J. W. Recent developments in cathode materials for lithium ion batteries. *J. Power Sources* **2010**, 195, 939-954.

12. Goodenough, J. B.; Kim,Y. Challenges for Rechargeable Li Batteries. *Chem. Mater.* **2010**, 22, 587-603.

13. Mizushima, K. J.; P.C.; Wiseman, P.J.; Goodenough, J.B. a new cathode materal for batteries of high energy density. *Mater. Res. Bull* **1980,** 15, 783-789.

14. Ozawa, K. Lithium-ion rechargeable batteries with $LiCoO_2$. *Solid State Ion.* **2002**, 69, 212-221.

15. Ohzuku, T.; Ueda, A. Why transition metal (di)oxides are the most attractive materials for batteries. *Solid State Ion.* **1994**, 69, 201-211.

16. Klaine, S. J.; Alvarez, P. J. J.; Batley, G. E.; Fernandes, T. F.; Handy, R. D.; Lyon, D. Y.; Mahendra, S.; Mclaughlin, M. J.; Lead, J. R. Nanomaterials in the environment behavior, fate, bioavailability. *Environ. toxicol. chem.* **2008**, 27, 1825-1851.

17. Xu, J. D.,; Liu, H.; Dai, L. Cathode materials for next generation lithium ion batteries. *Nano Energy* **2013**, 2, 439-442.

18. Wang, Y.; Gao, C. Developments in nanostructured cathode materials for high-performance lithium-ion batteries. *Adv. Mater.* **2008**, 20, 2251-2269.

19. Yi, T. F.; Li, X. Y.; Liu, H.; Shu, J.; Zhu,Y.R.; Zhu, R.S. Recent developments in the doping and surface modification of $LiFePO_4$ as cathode material for power lithium ion battery. *Ionics* **2012**, 18, 529-539.

20. Kim, D. K.; Muralidharan, P.; Lee, H.W.; Ruffo, R.; Yang, Y.; Chan, C. K.; Peng, H. Huggins, R. A. and Cui, Y. Spinel $LiMn_2O_4$ nanorods as lithium ion battery cathodes. *Nano Lett.* **2008**, 8, 3948-3952.

21. Yi, T. F.; Zhu, Y. R.; Zhu, X. D.; Shu, J.; Yue, C. B.; Zhou, A. N. A review of recent developments in the surface modification of $LiMn_2O_4$ as cathode material of power lithium-ion battery. *Ionics* **2009**, 15, 779-784.

22. Spahra, M. E.; Novak, P.; Schnydera, B.; Haasa, O.; Nesperb, R. Characterization of layered lithium nickel manganese oxides synthesized by a novel oxidative coprecipitation method and their electrochemical performance as lithium insertion electrode materials. *J. Electrochem. Soc.* **1998**, 145, 1113-1121.

23. Morcrette, M.; Rozier, P.; Dupont, L.; Mugnier, E.; Sannier, L. Galy, J.; Tarascon, J. M. A reversible copper extrusion-insertion electrode for Li batteries. *Nat. Mater.* **2003**, 2, 755-761.

24. Wu, X. Chang, S. H.; Park, Y. J. Ryu, K. S. Studies on capacity increase of $Li_{1.27}Cr_{0.2}Mn_{0.53}O_2$-based lithium batteries. *J. Power Sources* **2004**, 137, 105-110.

25. Zhang, L.; Wu, H. B.; Lou, X. W. D. Iron-oxide-based advanced anode for lithium-ion batteries. *Adv. Energy Mater.* **2014**, 4, 1300958-1300969.

26. Ma, J. Zhang, X.; Chen, K.; Li, G.; Han, X. Morphology-controlled synthesis of hematite hierarchical structures and their lithium storage performances. *J. Mater. Chem. A*, **2013**, 1, 5545-5553.

27. Wu, C.; Yin, P.; Zhu, X.; OuYang, C.; Xie, Y. Synthesis of hematite (α-Fe_2O_3) nanorods: diameter-size and shape effects on their applications in magnetism, lithium ion battery, and gas densors. *J. Phys. Chem. B* **2006**, 110, 17806-17812.

28. Wu, W. Wu, Z.; Yu, T.; Jiang, C.; Kim, W.S. Recent progress on magnetic iron oxide nanoparticles: synthesis, surface functional strategies and biomedical applications. *Sci. Technol. Adv. Mater.* **2016**, 16, 023501-023534.

29. Somogyvaari, Z.; Svab, E.; Maszaros, G.; Krezhov, K.; Nedkov, I.; Saja, I.; Boure, F. Vacancy ordering in nanosized maghemite from neutron and X-ray powder diffraction. *Appl. Phys. A.* **2002**, 74, 1077-1079.

30. Greaves, C. A powder neutron diffraction investigation of vacancy ordering and covalence in γ-Fe_2O_3. *J. Solid State Chem.* **1983**, 49, 325-333.

31. Korobeinikova, A.V.; Fadeeva, V. I.; Reznitskii, L. A. Study of the distribution of structural vacancies in γ-iron oxide. *J. Struct. Chem.* **1976**, 17, 737-741.

32. Belin, T. G.-M., N.; Caillot, T.; Aymes, D.; Niepce, J. C. Influence of grain size, oxygen stoichiometry, and synthesis conditions on the γ-Fe_2O_3 vacancies ordering and lattice parameters. *J. Solid State Chem.* **2002**, 163, 459-465.

33. Xu, J. S.; Zhu,Y. J. Monodisperse Fe_3O_4 and gamma-Fe_2O_3 magnetic mesoporous microspheres as anode materials for lithium-ion batteries. *ACS Appl. Mater. Interfaces* **2012**, 4, 4752-4757.

34. Long, J. W. Long, M. S.; Rhodes, C. P.; Carpenter, E. E.; Stroud, R. M. and Rolison, D. R. , Nanocrystalline iron oxide aerogels as mesoporous magnetic architectures. *J. Am. Chem. Soc.* **2004**, 126, 16879-16889.

35. Hahn, B. P. Long, J. W.; Rolison, D. R. Something from nothing enhancing electrochemical charge storage with cation vacancies. *Acc. Chem. Res.* **2013**, 46, 1181-1191.

36. Gasparov, L.V.Tanner, D. B.; Romero, D. B.; Berger, H.; Margaritondo, G.; Forró, L. Infrared and Raman studies of the verwey transition in magnetite. *Phys. Rev. B* **2000**, 62, 12-15.

37. El Mendili,Y.; Bardeau, J.F.; Randrianantoandro, N.; Grasset, F.; Greneche, J.M. Insights into the mechanism related to the phase transition from γ-Fe_2O_3 to α-Fe_2O_3 nanoparticles induced by thermal treatment and laser irradiation. *J. Phys. Chem. C* **2012**, 116, 23785-23792.

38. Randrianantoandro, N.; Mercier, A.M.; Hervieu, M.; Grene`che, J.M. Direct phase transformation from hematite to maghemite during high energy ball milling. *Mater. Lett.* **2001**, 47, 150-158.

39. Sun, Y.K.; Ma, M.; Zhang,Y.; Gu, N. Synthesis of nanometer-size maghemite particles from magnetite. *Colloids and Surfaces A: Physicochemical and Engineering Aspects* **2004**, 245, 15-19.

40. Kang, N.; Park, J. H.; Choi, J.; Jin, J.; Chun, J.; Jung, I. G.; Jeong, J.; Park, J. G.; Lee, S. M.; Kim, H. J.; Son, S. U. Nanoparticulate iron oxide tubes from microporous organic nanotubes as stable anode materials for lithium ion batteries. *Angew Chem. Int. Ed. Engl.* **2012**, 51, 6626-6630.

41. Cabana, J.; Monconduit, L.; Larcher, D.; Palacin, M. R. Beyond intercalation -based Li-ion batteries: the state of the art and challenges of electrode materials reacting through conversion reactions. *Adv. Mater.* **2010**, 22, 170-192.

42. Koo, B.; Xiong, H.; Slater, M. D.; Prakapenka,V. B.; Balasubramanian, M.; Podsiadlo, P.; Johnson, C. S.; Rajh, T.; Shevchenko, E. V. Hollow iron oxide nanoparticles for application in lithium ion batteries. *Nano Lett.*, **2012**, 12, 2429-2435.

43. Chen, Z.; Dahn, J. R. Methods to obtain excellent capacity retention in $LiCoO_2$ cycled to 4.5V. *Electrochim. Acta* **2004**, 49, 1079-1090.

44. Wu, X.L.; Jang, L.Y.; Cao, F.F.; Guo, Y.G.; Wan, L.J. $LiFePO_4$ nanoparticles embedded in a nanoporous carbon matrix: superior cathode material for electrochemical energy-storage devices. *Adv. Mater.* **2009**, 21, 2710-2714.

45. Kanzaki, S.; Inada, T.; Matsumura, T.; Sonoyama, N.; Yamada, A.; Takano, M.; Kanno, R. Nano-sized γ-Fe_2O_3 as lithium battery cathode. *J. Power Sources* **2005**, 146, 323-326.

46. Hahn, B. P.; Long, J. W.; Mansour, A. N.; Pettigrew, K. A.; Osofsky, M. S.; Rolison, D. R. Electrochemical Li-ion storage in defect spinel iron oxides the critical role of cation vacancies. *Energ. Environ. Sci.* **2011**, 4, 1495-1502.

47. Komaba, S.; Mikumo, T.; Ogata, A. Electrochemical activity of nanocrystalline Fe_3O_4 in aprotic Li and Na salt electrolytes. *Electrochem. Commun.* **2008**, 10, 1276-1279.

48. Gillot, B.; Nivoix,V. New cation-deficient vanadium–iron spinels with a high vacancy content. *Mater. Res. Bull.* **1999**, 34, 1735-1747.

49. Chervin, C. N.; Ko, J. S.; Miller, B. W.; Dudek, L.; Mansour, A. N.; Donakowski, M. D.; Brintlinger, T.; Gogotsi, P.; Chattopadhyay, S.; Shibata, T. Parker, J. F.; Hahn, B. P.; Rolison, D. R.; Long, J. W. Defective by design: iron oxide nanoarchitectures as cation-insertion hosts for electrochemical charge storage. *J. Mater. Chem. A* **2015**, 3, 12059-12068.

50. Larcher, D.; Masquelier, C.; Bonnin, D.; Chabre, Y.; Masson, V.; Leriche, J. B.; Tarascon, J. M. Effect of particle size on lithium intercalation into α-Fe_2O_3. *J. Electrochem. Soc* **2003**, 150, 133-139.

51. Kitaura, H.; Takahashi, K.; Mizuno, F.; Hayashi, A.; Tadanaga, K.; Tatsumisago, M., Preparation of α-Fe_2O_3 electrode materials via solution process and their electrochemical properties in all-solid-state lithium batteries. *J. Electrochem. Soc.* **2007**, 154, 725-729.

52. Liu, J.; Liu, X. W. Two-dimensional nanoarchitectures for lithium storage. *Adv. Mater.* **2012**, 24, 4097-4111.

53. Song, H.; Yu, L.; Lu, S.; Wang, T.; Liu, Z.; Yang, L. Remarkable differences in photoluminescent properties between $LaPO_4$:Eu one-dimensional nanowires and zero-dimensional nanoparticles. *Appl. Phys. Lett.* **2004**, 85, 470-472.

54. Ma, P. C.; Liu, M.Y.; Zhang, H.; Wang, S. Q.; Wang, R.; Wang, K.; Wong, Y. K.; Tang, B. Z.; Hong, S. H.; Paik, K. W.; Kim, J. K. Enhanced electrical conductivity of nanocomposites containing hybrid fillers of carbon nanotubes and carbon black. *ACS Appl. Mater. Interfaces* **2009**, 1, 1090-1096.

55. Butler, S. Z.; Hollen, S. M.; Cao, L.; Cui, Y.; Gupta, J. A.; Gutie´ rrez, H. R.; Heinz, T. F.; Huang, J.; Ismach, A. F.; Johnston-Halperin, E.; Kuno, M.; Plashnitsa, V. V.; Robinson, R. D.; Ruoff, R. S.; Salahuddin, S.; Shan, J.; Shi, L.; Spencer, O. M. G.; Terrones, M.; Windl, W.; Goldberger, J. E. Progress, challenges, and opportunities in two-dimensional materials beyond graphene. *Acs Nano* **2013**, 7, 2898-2926.

56. Wang, Q. H.; Kalantar-Zadeh, K.; Kis, A.; Jonathan N, C.; Strano, M. S.; Electronics and optoelectronics of two-dimensional transition metal dichalcogenides. *Nat. Nanotechnol.* **2012**, 7, 699-712.

57. Heine, T. Transition metal chalcogenides: ultrathin inorganic materials with tunable electronic properties. *Acc. Chem. Res.,* **2015**, 48, 65-72.

58. Ma, R.; Sasaki, T. Nanosheets of oxides and hydroxides: ultimate 2D charge-bearing functional crystallites. *Adv. Mater.* **2010**, 22, 5082-5104.

59. Dai, Z. R.; Pan, Z. W.; Wang, Z. L. Gallium oxide nanoribbons and nanosheets. *J. Phys. Chem. B* **2002**, 106, 902-904.

60. Yoo, E.; Kim, J.; Hosono, E.; Zhou, H. S.; Kudo, T.; Honma, I. Large reversible Li storage of graphene nanosheet families for use in rechargeable lithium ion batteries. *Nano Lett.* **2008**, 8, 2277-2282.

61. Bonaccorso, F.; Colombo, L.; Yu, G.; Stoller, M.; Tozzini, V.; Ferrari, A. C.; Ruoff, R. S.; Pellegrini, V. 2D materials. Graphene, related two-dimensional crystals, and hybrid systems for energy conversion and storage. *Science* **2015**, 347, 1246501-1246510.

62. Geim, A. K.; Novoselov, K. S. The rise of graphene. *Nat. Mater.* **2007**, 6, 183-191.

63. Lee, C.; Wei, X.; Kysar, J. W.; Hone, J. Measurement of the elastic properties and intrinsic strength of monolayer graphene. *Science* **2008**, 321, 385-388.

64. Park, S.; Ruoff, R. S. Chemical methods for the production of graphenes. *Nat. Nanotechnol.* **2009**, 4, 217-224.

65. Wang, Q. H.; Kalantar-Zadeh, K.; Kis, A.; Coleman, J. N.; Strano, M. S. Electronics and optoelectronics of two-dimensional transition metal dichalcogenides. *Nat. Nanotechnol.* **2012**, 7, 699-712.

66. Hilgenkamp, H.; Ariando; Smilde, H. J.; Blank, D. H.; Rijnders, G.; Rogalla, H.; Kirtley, J. R.; Tsuei, C. C. Ordering and manipulation of the magnetic moments in large-scale superconducting pi-loop arrays. *Nature* **2003**, 422, 50-53.

67. Chen, J. S.; Archer, L. A.; Xiong, W. L. SnO_2 hollow structures and TiO_2 nanosheets for lithium-ion batteries. *J. Mater. Chem.* **2011**, 21, 9912-9924.

68. Wang, C.; Zhou, Y.; Ge, M.; Xu, X.; Zhang, Z.; Jiang, J. Z. Large-scale synthesis of SnO_2 nanosheets with high lithium storage. *J. Am. Chem. Soc.* **2010**, 132, 46-47.

69. Hu, J.; Zhu, K.; Chen, L.; Yang, H.; Li, Z.; Suchopar, A.; Richards, R. Preparation and surface activity of single-crystalline NiO(111) nanosheets with hexagonal holes: a semiconductor nanospanner. *Adv. Mater.* **2008**, 20, 267-271.

70. Zhuiykov, S.; Kats, E. Atomically thin two-dimensional materials for functional electrodes of electrochemical devices. *Ionics* **2012**, 19, 825-865.

71. Mahmood, Q. K., M. G.; Yun, S.; Bak, S. M.; Yang, X. Q.; Shin, H. S.; Kim,W. S.; Braun, P. V.; Park, H. S., Unveiling surface redox charge storage of interacting two-dimensional heteronanosheets in hierarchical architectures. *Nano Lett.* **2015**, 15, 2269-2277.

72. Zhang, K.; Hu, S. H.; Zhang, Y.; Zhang, T. N.; Zhou, X. H.; Sun, Y.; Li, T. X.; Fan, H. J.; Shen, G. Z.; Chen, X. and Dai, N. Self-induced uniaxial strain in MoS_2 mono layers with local van der waals-stacked inter layer interactions. *Acs Nano* **2015**, 9, 2704-2710.

73. O'Dwyer, C.; Gannon, G.; McNulty, D.; Buckley, D. N.; Thompson, D. Accommodating curvature in a highly ordered functionalized metal oxide nanofiber: synthesis, characterization, and multiscale modeling of layered nanosheets. *Chem. Mater.* **2012**, 24, 3981-3992.

74. Kalantar-zadeh, K.; Vijayaraghavan, A.; Ham, M. H.; Zheng, H.; Breedon, M.; Strano, M. S. Synthesis of atomically thin WO_3 sheets from hydrated tungsten trioxide. *Chem. Mater.* **2010**, 22, 5660-5666.

75. Omomo, Y.; Sasaki, T.; Wang, L.; Watanabe, M. Redoxable nanosheet crystallites of MnO_2 derived via delamination of a layered manganese oxide. *J. Am. Chem. Soc.* **2003**, 125, 3568-3575.

76. Ma, R.; Takada, K.; Fukuda, K.; Iyi, N.; Bando, Y.; Sasaki, T. Topochemical synthesis of monometallic (Co^{2+}-Co^{3+}) layered double hydroxide and its exfoliation into positively charged $Co(OH)_2$ nanosheets. *Angew. Chem. Int. Ed. Engl.* **2008**, 47, 86-89.

77. Takagaki, A.; Yoshida, T.; Lu, D.; N. Kondo, J.; Hara, M.; Domen, K.; Hayashi, S. Titanium niobate and titanium tantalate nanosheets as strong solid acid catalysts. *J. Phys. Chem. B* **2004**, 108, 11549-11555.

78. Mas-Balleste, R.; Gomez-Navarro, C.; Gomez-Herrero, J.; Zamora, F. 2D materials: to graphene and beyond. *Nanoscale* **2011**, 3, 20-30.

79. Zhu, Y.; Cao, C.; Tao, S.; Chu, W.; Wu, Z.; Li, Y. Ultrathin nickel hydroxide and oxide nanosheets: synthesis, characterizations and excellent supercapacitor performances. *Sci. Rep.* **2014**, 4, 5787-5794.

80. Sun, Z.; Liao, T.; Dou, Y.; Hwang, S. M.; Park, M. S.; Jiang, L.; Kim, J. H.; Dou, S. X. Generalized self-assembly of scalable two-dimensional transition metal oxide nanosheets. *Nat. Commun.* **2014**, 5, 3813-3822.

81. Yang, H. G.; Liu, G.; Qiao, S. Z.; Sun, C. H.; Jin, Y. G.; Smith, S. C.; Zou, J.; Cheng, H. M.; Lu, G. Q. solvothermal synthesis and photoreactivity of Anatase TiO_2. *J. Am. Chem. Soc.* **2009**, 131, 4078-4083.

82. Sun, W.; Rui, X.; Zhu, J.; Yu, L.; Zhang, Y.; Xu, Z.; Madhavi, S.; Yan, Q. Ultrathin nickel oxide nanosheets for enhanced sodium and lithium storage. *J. Power Sources* **2015**, 274, 755-761.

83. Liu, Z.; Xu, K.; Sun, H.; Yin, S. One-Step synthesis of single-layer MnO_2 nanosheets with multi-role sodium dodecyl sulfate for high-performance pseudocapacitors. *Small* **2015**, 11, 2182-2191.

84. Cao, B.; Cai, W.; Li, Y.; Sun, F.; Zhang, L. Ultraviolet-light-emitting ZnO nanosheets prepared by a chemical bath deposition method. *Nanotechnology* **2005**, 16, 1734-1738.

85. Sun, Y.; Xia, Y. Shape-controlled synthesis of gold and silver nanoparticles. *Science* **2002**, 298, 2176-2179.

86. Sun, Y. Mayer, B.; Herricks, T.; Xia, Y. Polyol synthesis of uniform silver nanowires: a plausible growth mechanism and the supporting evidence. *Nano Lett.* **2003**, 3, 955-960.

87. Dong, R.; Hao, J. Aqueous surfactant-alcohol systems a review. *Chem. Rev.* **2010**, 110, 4978-5022.

88. Zana, R. Aqueous surfactant-alcohol systems A review. *Adv. Colloid Interface Sci.***1995**, 57, 61-64.

89. Fang, L.; Huang, L.; Holm, P. E.; Yang, X.; Hansen, H. B.; Wang, D. Facile upscaled synthesis of layered iron oxide nanosheets and their application in phosphate removal. *J. Mater. Chem. A* **2015**, 3, 7505-7512.

90. Hu, Y.; Qian, H.; Mei, T.; Guo, J.; White, T. Facile synthesis of magnetic metal (Mn, Co, Fe, and Ni) oxide nanosheets. *Mater. Lett.* **2010**, 64, 1095-1098.

91. Ma, M.; Zhang, Y.; Guo, Z.; Gu, N. Facile synthesis of ultrathin magnetic iron oxide nanoplates by Schikorr reaction. *Nanoscale Res. Lett.* **2013**, 8, 16-23.

92. Chen, P.; Xu, K.; Li, X.; Guo, Y.; Zhou, D.; Zhao, J.; Wu, X.; Wu, C.; Xie, Y. Ultrathin nanosheets of feroxyhyte: a new two-dimensional material with robust ferromagnetic behavior. *Chem. Sci.* **2014**, 5, 2251-2255.

93. Xu, C.; Zeng, Y.; Rui, X.; Zhu, J.; Tan, H.; Guerrero, A.; Toribio, J.; Bisquert, J.; Garcia-Belmonte, G.; Yan, Q. Amorphous iron oxyhydroxide nanosheets: synthesis, Li Storage, and conversion reaction kinetics. *J. Phys. Chem. C* **2013**, 117, 17462-17469.

94. Liu, D.; Wang, X.; Wang, X.; Tian, W.; Liu, J.; Zhi, C.; He, D.; Bando, Y.; Golberg, D. Ultrathin nanoporous Fe_3O_4-carbon nanosheets with enhanced supercapacitor performance. *J. Mater. Chem. A* **2013**, 1, 1952-1955.

95. Guan, N.; Sun, D.; Xu, J. Self-assembly of iron oxide nanoparticles into oriented nanosheets by one-pot template-free synthesis at low pH. *Mater. Lett.* **2009**, 63, 1272-1274.

96. Chen, Y. C.; Lin, Y. G.; Hsu, Y. K.; Yen, S. C.; Chen, K. H.; Chen, L. C. Novel iron oxyhydroxide lepidocrocite nanosheet as ultrahigh power density anode material for asymmetric supercapacitors. *Small* **2014**, 10, 3803-3810.

97. Kan, J.; Wang, Y. Large and fast reversible Li-ion storages in Fe_2O_3-graphene sheet-on-sheet sandwich-like nanocomposites. *Sci. Rep.* **2013**, 3, 3502-3512.

98. Bernal, J. D.; Dasgupta, D. R.; Mackay, A. L., the oxides and hydroxides of iron and their structural inter-relationships. *Clay Mineral Bulletin* **1959**, 4, 15-30.

99. Olowe, A. A.; Génin, J. M. R., The mechanism of oxidation of ferrous hydroxide in sulphated aqueous media: Importance of the initial ratio of the reactants. *Corros. Sci.* **1991**, 32, 965-984.

100. Pedrosa, J.; Costa, B. F. O.; Portugal, A.; Durães, L. Controlled phase formation of nanocrystalline iron oxides/ hydroxides in solution -An insight on the phase transformation mechanisms. *Mater. Chem. Phys.* **2015**, 163, 88-98.

101. Zhao, Y.; Peng, L.; Liu, B.; Yu, G. Single-crystalline $LiFePO_4$ nanosheets for high-rate Li-ion batteries. *Nano Lett.* **2014**, 14, 2849-2853.

102. Liu, S.; Jia, H.; Han, L.; Wang, J.; Gao, P.; Xu, D.; Yang, J.; Che, S. Nanosheet-constructed porous TiO_2-B for advanced lithium ion batteries. *Adv. Mater.* **2012**, 24, 3201-3204.

103. Cheng, F.; Tao, Z.; Liang, J.; Chen, J. Template-directed materials for rechargeable lithium-ion. *Chem. Mater.* **2008**, 20, 667-681.

104. Wu, M. S.; Ou, Y. H.; Lin, Y. P. Iron oxide nanosheets and nanoparticles synthesized by a facile single-step coprecipitation method for lithium-ion batteries. *J. Electrochem. Soc.* **2011**, 158, A231-A236.

105. Khorsand Zak, A.; Abd. Majid, W. H.; Abrishami, M. E.; Yousefi, R. X-ray analysis of ZnO nanoparticles by Williamson–Hall and size–strain plot methods. *Solid State Sci.* **2011**, 13, 251-256.

106. Shebanova, O. N.; Lazor, P. Raman study of magnetite (Fe_3O_4): laser- induced thermal effects and oxidation. *J.Raman Spectrosc.* **2003**, 34, 845-852.

107. Wang, F.; Liu, J.; Kong, J.; Zhang, Z.; Wang, X.; Itoh, M.; Machida, K. Template free synthesis and electromagnetic wave absorption properties of monodispersed hollow magnetite nano-spheres. *J. Mater. Chem.* **2011**, 21, 4314-4320.

108. Cheng, W.; Tang, K.; Qi, Y.; Sheng, J.; Liu, Z. One-step synthesis of superparamagnetic monodisperse porous Fe3O4 hollow and core-shell spheres. *J. Mater. Chem.* **2010**, 20, 1799-1805.

109. Kakuta, S.; Numata, T.; Okayama, T. Shape effects of goethite particles on their photocatalytic activity in the decomposition of acetaldehyde. *Catal. Sci. Technol.* **2014**, 4, 164-169.

110. Zboril, R.; Mashlan, M.; Petridis, D. Iron(III) oxides from thermal processess synthesis, structural and magnetic properties, Mossbauer spectroscopy characterization, and applications. *Chem. Mater.* **2002**, 14, 969-982.

111. Cao, S. W.; Zhu, Y. J.; Ma, M. Y.; Li, L.; Zhang, L. Hierarchically nanostructured magnetic hollow spheres of Fe_3O_4 and gamma-Fe_2O_3 preparation and potential application in drug delivery. *J. Phys. Chem. C* **2008**, 112, 1851-1856.

112. Lu, J.; Jiao, X. L.; Chen, D.; Li, W. Solvothermal synthesis and characterization of Fe_3O_4 and γ-Fe_2O_3 nanoplates. *J. Phys. Chem. C* **2009**, 113, 4012-4017.

113. Long, J. W.; Logan, M. S.; Rhodes, C. P.; Carpenter, E. E.; Stroud, R. M.; Rolison, D. R. Nanocrystalline iron oxide aerogels as mesoporous magnetic architectures. *J. Am. Chem. Soc.* **2004**, 126, 16879-16889.

114. Darezereshki, E. One-step synthesis of hematite (α-Fe_2O_3) nano-particles by direct thermal-decomposition of maghemite. *Mate. Lett.* **2011**, 65, 642-645.

115. Azadmanjiri, J.; Simon, G.P.; Suzuki, K.; Selomulya, C. Cashion, J. D. Phase reduction of coated maghemite (γ-Fe_2O_3) nanoparticles under microwave-induced plasma heating for rapid heat treatment. *J. Mater. Chem.* **2012**, 22, 617-625.

116. Roonasi, P.; Holmgren, A., A Fourier transform infrared (FTIR) and thermogravimetric analysis (TGA) study of oleate adsorbed on magnetite nano-particle surface. *Appl. Surf. Sci.* **2009**, 255, 5891-5895.

117. Lu, J. F.; Tsai, C. J. Hydrothermal phase transformation of hematite to magnetite. *Nanoscale Res. Lett.* **2014**, 9, 230-238.

118. Monshi, A.; Foroughi, M. R.; Monshi, M. R. Modified Scherrer equation to estimate more accurately nano-crystallite size using XRD. *World Journal of Nano Science and Engineering* **2012**, 2, 154-160.

119. Reddy, M. V.; Yu, T.; Sow, C. H.; Shen, Z. X.; Lim, C. T.; Subba Rao, G. V.; Chowdari, B. V. R. α-Fe_2O_3 nanoflakes as an anode material for Li-ion batteries. *Adv. Funct. Mater.* **2007**, 17, 2792-2799.

120. Zhou, G. W., D.-W.; Li, F.; Zhang, L.; Li, N.; Wu, Z.-S.; Wen, L.; Lu, G.Q.; Cheng, H.-M., Graphene-wrapped Fe_3O_4 anode material with improved reversible capacity and cyclic stability for lithium ion batteries. *Chem. Mater.* **2010**, 22, 5306-5313.

121. Hahn, B. P.; Long, J. W.; Mansour, A. N.; Pettigrew, K. A.; Osofskyd, M. S.; Rolison, D. R. Electrochemical Li-ion storage in defect spinel iron oxides the critical role of cation vacancies. *Energy Environ. Sci.* **2011**, 4, 1495-1502.

122. Gillot, B.; Nivoix, V. New cation-deficient vanadium–iron spinels with a high vacancy content. *Mater. Res. Bull.* **1999**, 34, 1735-1747.

123. Chiang, Y.-C.; Chiang, P.-C.; Huang, C.-P. Effects of pore structure and temperature on VOC adsorption on activated carbon. *Carbon* **2001**, 39, 523-534.

124. Wu, L.; Yao, H.; Hu, B.; Yu, S.-H. Unique lamellar sodium/potassium iron oxide nanosheets: facile microwave-assisted synthesis and magnetic and electrochemical properties. *Chem. Mater.* **2011**, 23, 3946-3952.

125. Augustyn, V.; White, E. R.; Ko, J.; Grüner, G.; Regan, B. C.; Dunn, B. Lithium-ion storage properties of titanium oxide nanosheets. *Mater. Horiz.* **2014**, 1, 219-223.

126. Zhang, S. M.; Zhang, J. X.; Xu, S. J.; Yuan, X. J.; He, B. C. Li ion diffusivity and electrochemical properties of FePO4 nanoparticles acted directly as cathode materials in lithium ion rechargeable batteries. *Electrochim. Acta* **2013**, 88, 287-293.

127. Padhi, A. K.; Nanjundaswamy, K. S.; Masquelier, C.; Okada, S.; Goodenough, J. B. Effect of structure on the Fe^{3+}/Fe^{2+} redox couple in iron phosphates. *J. Electrochem. Soc.* **1997**, 144, 1609-1613.

128. Lindstro, H.; Sodergren, S.; Solbrand, A.; Rensmo, H.; Hjelm, J.; Hagfeldt, A.; Lindquist, S.E. Li^+ ion insertion in TiO_2 (anatase). 2. Voltammetry on nanoporous films. *J. Phys. Chem. B* **1997**, 101, 7717-7722.

129. Augustyn, V.; White, E. R.; Ko, J.; Grüner, G.; Regan, B. C.; Dunn, B. Lithium-ion storage properties of titanium oxide nanosheets. *Mater. Horiz.* **2014**, 1, 219-223.